Neuron

Article

Human cortical neurogenesis is altered via glucocorticoid-mediated regulation of ZBTB16 expression

Graphical abstract

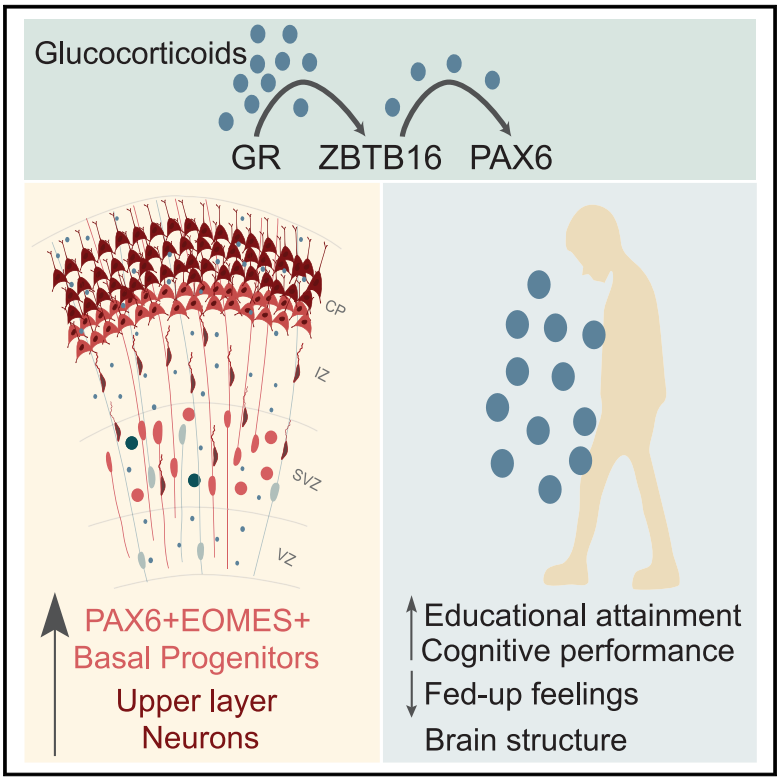

Authors

Anthi C. Krontira, Cristiana Cruceanu, Leander Dony, ..., Marta Labeur, Silvia Cappello, Elisabeth B. Binder

Correspondence

anthi.krontira@bmc.med.lmu.de (A.C.K.), binder@psych.mpg.de (E.B.B.)

In brief

Krontira et al. study the effects of glucocorticoids on neurogenesis in human cerebral organoids and mice. They find that glucocorticoids, via *ZBTB16*, increase PAX6^{+}EOMES^{+} basal progenitors, a cell type enriched in species with a gyrified brain, and upper-layer neurons. This is associated with beneficial postnatal outcomes such as enhanced cognitive performance.

Highlights

- Glucocorticoids increase PAX6^{+}EOMES^{+} basal progenitors and upper-layer neurons
- ZBTB16 is necessary and sufficient for the glucocorticoid effects on neurogenesis
- ZBTB16 activates gyrified species-enriched processes in a lissencephalic cortex
- Glucocorticoid excess during neurogenesis relates to beneficial postnatal outcomes

Krontira et al., 2024, Neuron *112*, 1426–1443
May 1, 2024
https://doi.org/10.1016/j.neuron.2024.02.005

CellPress

CellPress
OPEN ACCESS

Neuron

Article

Human cortical neurogenesis is altered via glucocorticoid-mediated regulation of ZBTB16 expression

Anthi C. Krontira,[1,2,17,18,*] Cristiana Cruceanu,[1,3] Leander Dony,[1,2,7,8] Christina Kyrousi,[4,5,6] Marie-Helen Link,[1] Nils Rek,[1,2] Dorothee Pöhlchen,[1,2] Catarina Raimundo,[1] Signe Penner-Goeke,[1] Alicia Schowe,[1,9] Darina Czamara,[1] Marius Lahti-Pulkkinen,[10,11,12] Sara Sammallahti,[13] Elina Wolford,[10] Kati Heinonen,[10,14,15] Simone Roeh,[1] Vincenza Sportelli,[1] Barbara Wölfel,[1] Maik Ködel,[1] Susann Sauer,[1] Monika Rex-Haffner,[1] Katri Räikkönen,[10] Marta Labeur,[1] Silvia Cappello,[4,16] and Elisabeth B. Binder[1,18,19,20,*]

[1]Department Genes and Environment, Max Planck Institute of Psychiatry, Munich 80804, Germany
[2]International Max Planck Research School for Translational Psychiatry, Munich 80804, Germany
[3]Department of Physiology and Pharmacology, Karolinska Institutet, Stockholm 17177, Sweden
[4]Developmental Neurobiology, Max Planck Institute of Psychiatry, Munich 80804, Germany
[5]First Department of Psychiatry, Medical School, National and Kapodistrian University of Athens, Eginition Hospital, Athens 15784, Greece
[6]University Mental Health, Neurosciences and Precision Medicine Research Institute "Costas Stefanis", Athens 15601, Greece
[7]Department for Computational Health, Helmholtz Munich, Neuherberg 85764, Germany
[8]TUM School of Life Sciences Weihenstephan, Technical University of Munich, Freising 85354, Germany
[9]Graduate School of Systemic Neurosciences, Ludwig-Maximilians-University, Munich 82152, Germany
[10]Department of Psychology and Logopedics, Faculty of Medicine, University of Helsinki, Helsinki 00014, Finland
[11]Finnish Institute for Health and Welfare, Helsinki 00271, Finland
[12]Centre for Cardiovascular Science, Queen's Medical Research Institute, University of Edinburgh, Edinburgh EH16 4TJ, UK
[13]Department of Obstetrics and Gynecology, Helsinki University Hospital and University of Helsinki, Helsinki 00014, Finland
[14]Psychology/Welfare, Faculty of Social Sciences, University of Tampere, Tampere 33014, Finland
[15]Lawrence S. Bloomberg Faculty of Nursing, University of Toronto, Toronto, ON M5T 1P8, Canada
[16]Physiological Genomics, Biomedical Center (BMC), Faculty of Medicine, Ludwig-Maximilians-University (LMU), Munich 82152, Germany
[17]Present address: Institute of Stem Cell Research, Helmholtz Center Munich, German Research Center for Environmental Health & Physiological Genomics, Biomedical Center (BMC), Faculty of Medicine, Ludwig-Maximilians-University (LMU), Munich 82152, Germany
[18]These authors contributed equally
[19]Senior author
[20]Lead contact
*Correspondence: anthi.krontira@bmc.med.lmu.de (A.C.K.), binder@psych.mpg.de (E.B.B.)
https://doi.org/10.1016/j.neuron.2024.02.005

SUMMARY

Glucocorticoids are important for proper organ maturation, and their levels are tightly regulated during development. Here, we use human cerebral organoids and mice to study the cell-type-specific effects of glucocorticoids on neurogenesis. We show that glucocorticoids increase a specific type of basal progenitors (co-expressing PAX6 and EOMES) that has been shown to contribute to cortical expansion in gyrified species. This effect is mediated via the transcription factor ZBTB16 and leads to increased production of neurons. A phenome-wide Mendelian randomization analysis of an enhancer variant that moderates glucocorticoid-induced *ZBTB16* levels reveals causal relationships with higher educational attainment and altered brain structure. The relationship with postnatal cognition is also supported by data from a prospective pregnancy cohort study. This work provides a cellular and molecular pathway for the effects of glucocorticoids on human neurogenesis that relates to lasting postnatal phenotypes.

INTRODUCTION

Prenatal development affects postnatal health. The "developmental origin of health and disease (DOHaD) hypothesis"[1] proposes that environmental exposures during critical prenatal periods have lasting effects on cells and tissues, including on the central nervous system (CNS),[2] impacting lifelong human health.

Glucocorticoids (GCs) are steroid hormones that play a vital role in CNS development during pregnancy.[3] GCs regulate

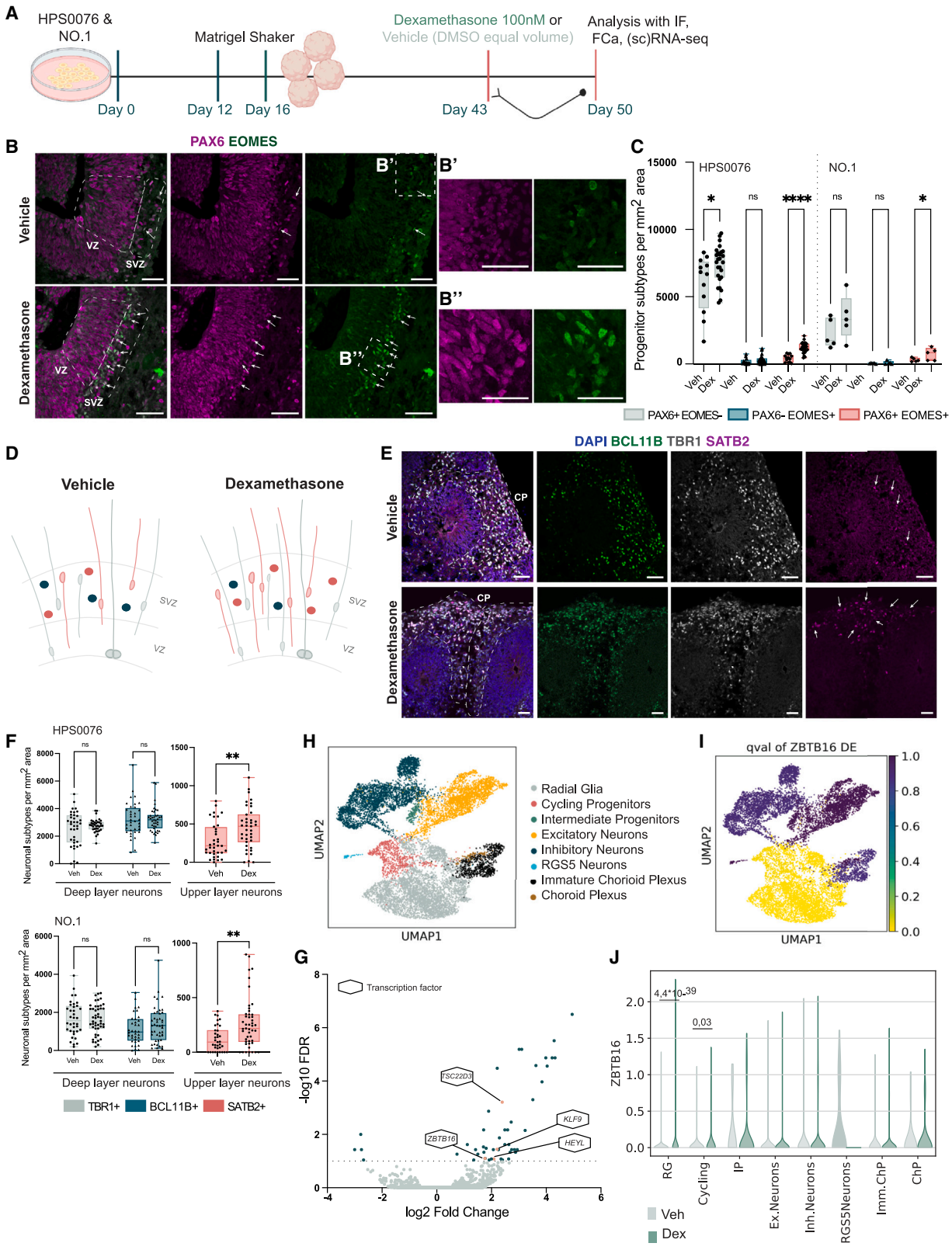

(legend on next page)

fetal organ development, particularly for the lungs and brain.[4] Their levels are very tightly regulated during gestation in a species-specific pattern. Corticosterone, the main GC in mice, increases sharply late in gestation, whereas the levels of cortisol, the main GC in humans, rise progressively starting at the beginning of the second trimester.[5]

GC levels outside the physiological range and/or time window, resulting from the therapeutic use of synthetic GCs (sGCs) or from maternal endocrine and stress-related disorders, impact fetal development.[3] The placenta acts as a protective barrier for endogenous maternal GCs, but stress and depression can reduce placental cortisol metabolism.[6] Furthermore, sGCs readily cross the placenta,[7] leading to higher exposure of the fetus. sGCs, either betamethasone or dexamethasone (dex), are most commonly prescribed from 22 to 33 gestational weeks (GWs) in pregnancies at high risk for preterm delivery to facilitate fetal lung maturation, increasing survival rates.[8,9] More than 1 in 10 babies are born prematurely every year, a number that amounts to ~15 million preterm births (<GW37),[10] of which ~615,000 are born extremely preterm (<GW28),[11] highlighting the clinical and societal importance of prenatal sGC use.

Deviation from the physiological range of prenatal GCs can have lasting postnatal effects on brain structure and behavior, as seen in large epidemiological studies,[12] and data from animal models support direct GC effects.[3] In fact, although the molecular and cellular effects of GCs on the term and adult brain are well characterized in rodents,[13] their impact on early brain development, especially during the human neurogenic period (extending until GW28[14] in humans and thus in the time frame of sGC administration for extremely preterm births), remains largely unexplored.

To address this, we combined experiments in human cerebral organoids (hCOs) and mouse embryos with human genetic analyses and mechanistically linked enhanced prenatal sGC exposure to human cortical neurogenesis and lasting effects on cognitive abilities and brain structure.

RESULTS

GCs increase the number of basal progenitors

To study GC regulation of neurogenic trajectories in the neocortex, we treated hCOs[15] with 100 nM dex for 7 days, a dose and time consistent with therapeutic guidelines followed in clinical settings[8] (see STAR Methods). This treatment was initiated at day 43 (Figure 1A) in hCOs derived from two independent induced pluripotent stem cell (iPSC) lines, HPS0076 and No.1. Days 40–50 were chosen as a time range for when hCOs are actively performing neurogenic processes with all the progenitor cell types present while the birth of deep-layer neurons is peaking and the birth of upper-layer neurons has started.[16] First, we analyzed the effects of dex on different progenitor cell types defined by the expression of paired box 6 (PAX6) and eomesodermin (EOMES, also known as T-box brain protein 2 or TBR2). PAX6 is highly expressed in radial glia (RG) cells; EOMES, but not PAX6, is expressed in intermediate basal progenitors (IPs); whereas both can be expressed in certain basal progenitors (BPs). Dex consistently led to a significant increase of $PAX6^+EOMES^+$ BPs (Figures 1B and 1C) in hCOs derived from both iPSC lines. These $PAX6^+EOMES^+$ cells were localized at the basal side of the germinal zones in the subventricular-like zone (SVZ; Figures 1D, S1A, and S1B). Moreover, we confirmed these effects of dex by analyzing the number of progenitor subtypes in No.1 hCOs with flow cytometry analysis (FCa). We observed a significant increase (+11%) in $PAX6^+EOMES^+$ BPs when hCOs were treated with dex compared with vehicle (veh; Figures S2A–S2C). Co-administration of the GC receptor (GR) antagonist RU486 supported that dex effects are mainly mediated by the GR and not the mineralocorticoid receptor (Figures S2D–S2F). Furthermore, the increased numbers of these BPs seem to contribute to germinal layer expansion as seen by increased $PAX6^+$ zone thickness in dex-treated ventricles (Figure S1C).

To further study the effects of dex on $PAX6^+EOMES^+$ BPs at the RNA level, we analyzed single-cell RNA sequencing

Figure 1. Glucocorticoids increase basal progenitors that co-express PAX6 and EOMES

(A) Treatment and analysis workflow.

(B) Representative images of day 50 hCOs at veh and dex conditions stained for PAX6 and EOMES. Arrows indicate cells that co-express PAX6 and EOMES. (B′ and B″) Zoomed-in images of the areas.

(C) Quantification of the progenitor subtypes in each treatment condition normalized by mm^2 of quantified total area in HPS0076 hCOs on the left and No.1 hCOs on the right.

(D) Schematic representation of the effects of dex on progenitors, highlighting the increased numbers of BPs co-expressing PAX6 and EOMES.

(E) Representative images of day 50 hCOs at veh and dex conditions stained for $TBR1^+$, $BCL11B^+$, and $SATB2^+$ neurons and DAPI. Arrows indicate $SATB2^+$ neurons in the CP.

(F) Quantification of neuronal subtypes found in the CP normalized per mm^2 of area in HPS0076 hCOs on the top and No.1 hCOs on the bottom.

(G) Volcano plot of DE analysis in bulk RNA-seq. Gray dots, genes with non-significant expression changes at an FDR cutoff of 10%; blue dots, genes with significant expression changes; orange dots, TFs labeled with their gene name.

(H) Single-cell clusters of HPS0076 hCOs treated with 100 nM dex for 10 days starting at day 60.

(I) UMAP plot showing *ZBTB16* FDR value of dex response per cluster.

(J) Violin plot of *ZBTB16* expression changes per cluster.

FDR, false discovery rate with Benjamini-Hochberg correction; DMSO, dimethyl sulfoxide; IF, immunofluorescence; Seq, sequencing; Veh, vehicle; Dex, dexamethasone; VZ, ventricular-like zone; SVZ, subventricular-like zone; BPs, basal progenitors; CP, cortical-like plate; TFs, transcription factors; RG, radial glia; Cycling, cycling progenitors; IP, intermediate progenitors; Ex. Neurons, excitatory neurons; Inh. Neurons, inhibitory neurons; Imm. ChP, immature choroid plexus; ChP, choroid plexus. Significance was tested with two-tailed Mann-Whitney comparison between treatment and vehicle. Box and whisker plots represent 25^{th} to 75^{th} percentile of the data with the center line representing the median and whiskers representing minima and maxima. ****$p \leq 0.0001$, **$p \leq 0.01$, *$p \leq 0.05$, ns $p > 0.05$. Scale bars, 50 μm.

See also Figures S1 and S2 and Tables S2 and S3–S5.

(scRNA-seq) data of HPS0076 hCOs treated with 100 nM dex for 10 days (treatment initiation at day 60). We found a 3.38-fold increase in PAX6$^+$EOMES$^+$ cells after dex, similar to the fold changes we found with our immunostainings (Figure S1D; Table S3). We sub-setted our dataset to the PAX6$^+$EOMES$^+$ cells and performed differential expression (DE) analysis for treatment effects on those. We found only two DE genes significant at a false discovery rate (FDR) threshold of 10%, *MEST* and *RSPO3* (Table S2), which are both WNT signaling regulators and very important for neurodevelopmental decisions associated with the dorso-ventral axis and the production of glutamatergic neurons.[17,18] In addition, there were 221 DE genes significant at the nominal p value level of <0.05. We performed gene set enrichment analysis (GSEA) to identify gene sets overrepresented in the PAX6$^+$EOMES$^+$ cells after treatment. We uncovered gene sets associated with cell fate commitment and glial cell proliferation and differentiation (Figure S1E; Table S2), highlighting the importance of these cells in regulating neurogenic processes and their potential ontological association with RG cells.

We next sought to characterize GC effects on neuronal populations. We labeled deep-layer VI and V neurons with T-box brain transcription factor (TBR1) and BAF chromatin remodeling complex subunit (BCL11B, also known as CTIP2), respectively, and upper-layer IV neurons with SATB homeobox 2 (SATB2; Figure 1E). Dex consistently led to a significant increase of upper-layer SATB2$^+$ neurons in hCOs from both iPSC lines compared with veh-treated ones. No significant change was found in deep-layer neurons (Figure 1F). To further validate these results, we used FCa and found increased numbers of upper-layer IV neurons (SATB2$^+$ cells, a 9% significant increase; Figures S2G and S2H) following dex. In addition, dex led to an increase of immature neuronal somata (doublecortin [DCX$^+$]) at the basal parts of the germinal zone and to a decrease of the DCX zone thickness in the cortical-like plate (CP; Figures S2I–S2K), potentially pointing to later-born neurons still migrating to their final destination.

This putatively prolongated neurogenesis could be related to the increased numbers of PAX6$^+$EOMES$^+$ BPs. These BPs have high proliferative capacity, undergoing not only neurogenic but also self-renewing proliferative divisions, which come in contrast to PAX6$^-$EOMES$^+$ IPs that primarily undergo one neurogenic division producing two neurons.[19–24] Interestingly, PAX6$^+$EOMES$^+$ BPs are abundant in the inner and outer SVZ of mammals with a gyrified brain, such as ferrets, primates, and humans, and contribute to the increased neurogenic potential of these species.[20] In lissencephalic species, like rodents, this cell type is rare, with the vast majority of BPs being IPs.[19–24] Overall, GCs seem to increase neurogenic processes that are enriched in gyrified species.

Transcriptional response to GCs during neurogenesis

Next, we aimed to identify genes and pathways responsible for the effects of GCs on neurogenesis. For this, we first used bulk RNA-seq of No.1 day 45 hCOs treated with 100 nM dex or veh for 7 days (treatment start at day 38). At a 10% FDR cutoff, 50 genes were DE (Table S2). Given the essential role and developmental specificity of transcription factors (TFs) in determining neurodevelopmental processes,[25] we decided to focus on this class of proteins. Out of the 50 DE genes, only 4 were TFs: TSC22 domain family member 3 (*TSC22D3*), Kruppel-like factor 9 (*KLF9*), zinc finger and BTB domain-containing protein 16 (*ZBTB16*), and HEY-like protein (*HEYL*; Figure 1G). To narrow in on progenitor-specific responses, we used two scRNA-seq datasets. First, to define the cell-type-specific expression of these TFs early during neurogenesis, we used an already published dataset of No.1 day 30 hCOs.[16] *HEYL* and *KLF9* were very lowly expressed in the majority of cell types, *TSC22D3* was found across all cell types, and only the expression of *ZBTB16* coincided with *PAX6*-positive cells (Figures S3A and S3B; Table S3). Second, to study progenitor-specific effects of chronic dex exposure, we used the aforementioned scRNA-seq dataset of HPS0076 hCOs with 10-day dex stimulation. At an FDR cutoff of 5%, we found 3,320 significantly DE genes in progenitors, one of which was *PAX6* (FDR = 3.53×10^{-13}, $\log_2$ fold change = 0.190), and 1,869 DE genes in non-progenitor cells (neuronal and choroid plexus cells; Table S2). Overrepresentation analysis for Gene Ontology Biological Processes pinpointed significant enrichments for terms associated with cellular proliferation, metabolism, and adhesion/mobility in the progenitor DE genes, supporting the effects of dex on progenitor amplification. In neuronal and choroid cells, we found significantly enriched terms associated with neurogenesis and differentiation, again highlighting the importance of dex in regulating neurogenic processes (Table S2). *ZBTB16* was differentially overexpressed exclusively in the progenitors' clusters (Figures 1H–1J; Table S4) and was, thus, the strongest candidate for dex effects on neural progenitors. Additionally, *ZBTB16* binding sites were enriched in the progenitor-specific DE genes, highlighting the importance of this TF for the effects of dex on progenitors. Among the genes that are ZBTB16 targets and DE in progenitor cells are *ZBTB16* itself but also *TP53*, which has been shown to regulate neural stem and progenitor cell proliferation and neurogenesis,[26] and *CRABP1*, a retinoic acid signaling protein found enriched in progenitor cells[27] (Table S5). *ZBTB16* has been associated with regulation of the balance between self-renewal and differentiation of stem and progenitor cells in multiple organ systems including the brain.[28]

GCs alter the very dynamic neurodevelopmental expression pattern of ZBTB16

In rodents, Zbtb16 is expressed until embryonic day 10.5 (E10.5) in the forebrain,[29] when it is downregulated to non-detectable levels during neurogenesis (Figures S3C and S3D). By contrast, in human fetal cortex, ZBTB16 is expressed during the initial stages of neurogenesis (Figure S3E), indicating presence during the neurogenic period in humans but not in rodents.

We first analyzed the pattern of ZBTB16 expression in the hCOs. We found it dynamically expressed with high RNA (Figure 2A) and protein (Figure 2B) levels at early stages of hCO development until approximately day 40, with a subsequent decrease once mature neurons emerge (microtubule-associated protein 2 [MAP2$^+$] cells) (day 50; Figure 2A). ZBTB16 was enriched in the germinal zones, mainly expressed by progenitor cells (SRY-box transcription factor 2 [SOX2$^+$] cells) and not expressed by mature neurons (MAP2$^+$; Figure 2C). Thus, *ZBTB16*

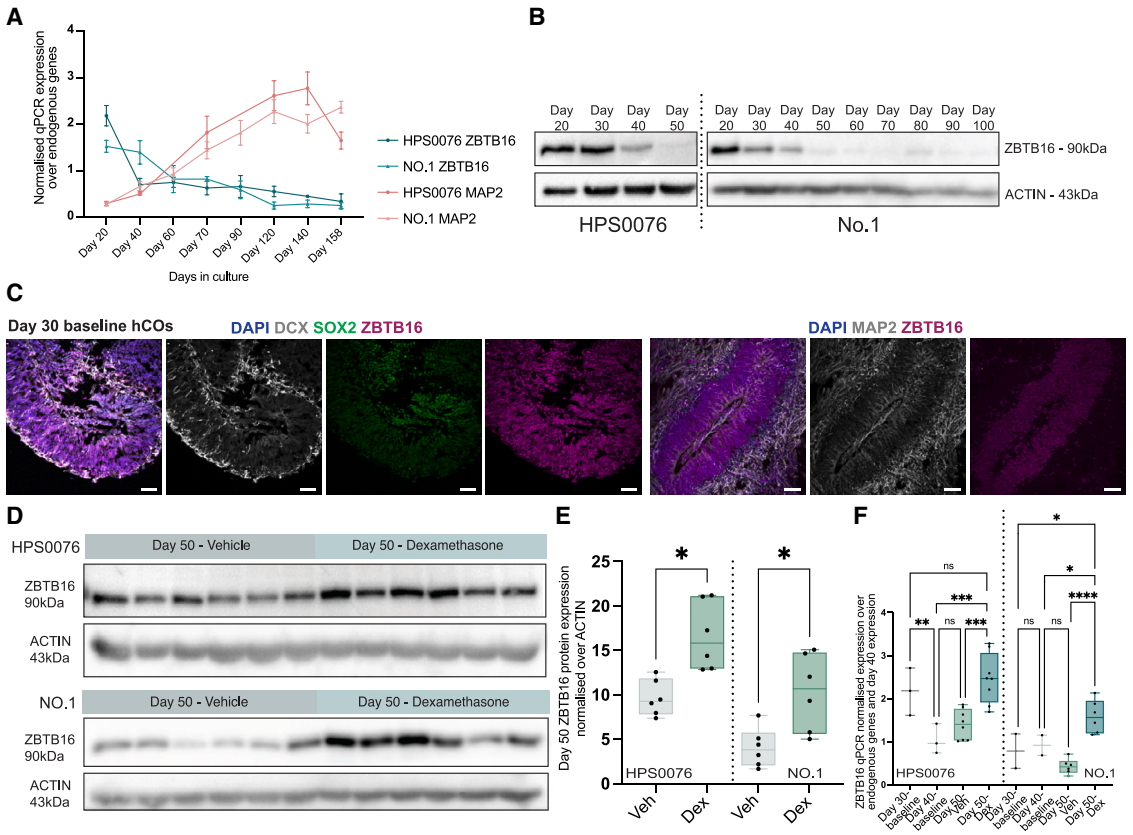

Figure 2. Glucocorticoids alter the expression profile of ZBTB16

(A) RT-qPCR results for *ZBTB16* and *MAP2* across hCO development.

(B) Western blots of ZBTB16 and ACTIN across hCO development. Each lane contains protein from a pool of three hCOs.

(C) Representative images of day 30 baseline hCOs stained for DCX, SOX2, MAP2, ZBTB16, and DAPI.

(D) Western blots of ZBTB16 and ACTIN in hCOs treated with 100 nM dex at day 43 and analyzed 7 days later at day 50. Each lane contains protein from a pool of three hCOs, and the six replicates were generated in two independent hCO batches.

(E) Quantification of the effect of 100 nM dex over 7 days on ZBTB16 protein expression in day 50 hCOs normalized over ACTIN.

(F) Quantification of the effect of 100 nM dex over 7 days on *ZBTB16* mRNA levels normalized over endogenous genes and day 40 baseline *ZBTB16* expression levels.

RT-qPCR, quantitative reverse-transcription polymerase chain reaction; hCOs, human cerebral organoids; Veh, vehicle; Dex, dexamethasone. For (E), significance was tested with two-tailed Mann-Whitney comparison between treatment and vehicle. For (F), significance was tested with one-way ANOVA with Benjamini, Krieger, and Yekutieli multiple testing correction ($p = 0.0003$). Box and whisker plots represent 25th to 75th percentile of the data with the center line representing the median and whiskers representing minima and maxima. Mann-Whitney p values for (E) or post hoc p values for (F): ****$p \leq 0.0001$, ***$p \leq 0.001$, **$p \leq 0.01$, *$p \leq 0.05$, ns $p > 0.05$. Scale bars, 50 μm.

See also Figure S3.

exhibits a very dynamic expression pattern in hCOs with high protein expression during the initial period of neurogenesis, consistent with data reported from human fetal cortex (Figure S3E).

We next took advantage of the 10-day scRNA-seq data to investigate the effects of *ZBTB16* expression on the transcriptional signature of progenitor cells. We sub-setted our dataset to the progenitor clusters at veh and performed a DE analysis for ZBTB16-positive vs. -negative cells (Table S2). We found 442 DE genes at a nominal p value cutoff of 0.05, one of which was *PAX6* (p value = 0.003, $\log_2$ fold change = 0.348). GSEA revealed significantly enriched gene sets associated with neuron differentiation, regulation of microtubule organization, and transcription, highlighting the importance of *ZBTB16* in regulating proliferative and neurogenic processes (Figure S3F; Table S2).

Finally, we validated the dex-induced increase of ZBTB16 in hCOs (100 nM dex for 7 days starting at day 43; Figure S3G) at the RNA (Figure S3H, similar to our previous report after 4- and 12-h dex treatments[16]) and protein (Figures 2D and 2E) levels in the progenitor cells that line the ventricular-like zone (VZ; Figures S3I and S3J). Dex alters the tightly regulated developmental expression pattern of this TF by reversing its levels to those of day 30 and younger hCOs (Figure 2F). Together, these results suggest that dex maintains high ZBTB16 expression in the progenitor cells that populate the germinal zones during later

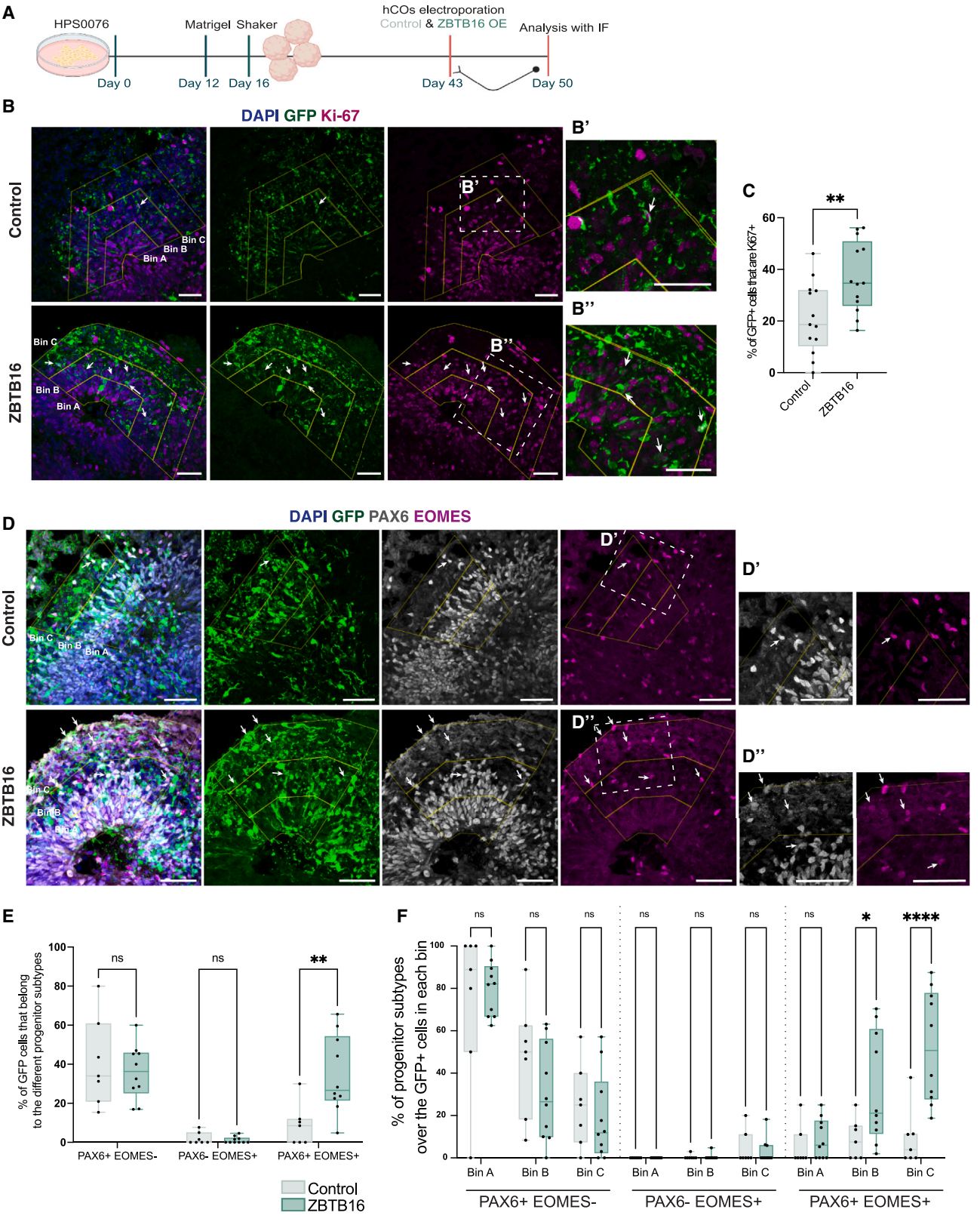

(legend on next page)

stages of neurogenesis, at developmental time windows with physiologically lower levels of this TF.

ZBTB16 mimics the effects of GCs on basal progenitors

To test whether the effects of dex on BPs are mediated via ZBTB16, we overexpressed ZBTB16 and green fluorescent protein (GFP) from a bicistronic plasmid or GFP from a control plasmid in hCOs starting at day 43 when ZBTB16 expression is already declining (Figures 2A and 2B). Subsequent analyses were performed 7 days after the electroporation, at day 50 (Figure 3A). To explore effects on progenitor subtypes of the VZ and the SVZ and on neurons of the CP, we divided the electroporated area into three bins of equal height, starting from the apical-most part of the VZ to the outermost electroporated cell in the CP and analyzed effects on GFP^+ cells. In these analyses, the germinal zone thickness did not differ between control- and ZBTB16-electroporated ventricles, ensuring consistent bin formation (Figure S4A).

ZBTB16 overexpression led to increased numbers of Ki-67^+ cells (Figures 3B and 3C), indicating an increase in proliferation potential. In analogy with our dex experiments, we next co-analyzed PAX6 and EOMES expression. Indeed, ZBTB16 overexpression led to a similar phenotype to that of dex, with an overall 25.7% increase in $PAX6^+EOMES^+$ BPs (Figures 3D and 3E) in bins B and C, +23.8% and +43.1%, respectively (Figure 3F), which reflect the basal parts of the VZ, the SVZ, and the CP. Using GFP cell morphology reconstructions, we found the double-positive BPs exhibiting both IP-related morphologies with no processes and RG-related morphologies with unipolar or bipolar cells (Figure S4B), similar to what has been described before for these double-positive cells in macaques and humans.[20,30] ZBTB16 overexpression thus increases the relative abundance of $PAX6^+EOMES^+$ BPs but does not bias them toward any specific morphology ($p = 0.23$; Figure S4C).

We next studied the effects of ZBTB16 overexpression on deep-layer $BCL11B^+$ and upper-layer $SATB2^+$ neurons. We found a significant 19% increase of $SATB2^+$ cells after ZBTB16 overexpression, whereas the effect on $BCL11B^+$ deep-layer neurons was less pronounced (a non-significant 11% increase; Figures S4D–S4F), indicating increased upper-layer neuronal production. Thus, similar to dex (Figures 1E and 1F), ZBTB16 overexpression increases the number of double-positive BPs and upper-layer neurons.

ZBTB16 is necessary for the effects of GCs on basal progenitors

We next sought to determine whether ZBTB16 is, in fact, necessary for the dex-induced phenotype. To achieve this, we used CRISPR-Cas9 to knock out exon 2 of the *ZBTB16* locus in the No.1 iPSCs. Exon 2 encodes for more than 50% of the protein and includes the initiating ATG, the BTB/POZ domain, and the first two zinc fingers of the binding domain.[31] We created heterozygous No.1 iPSCs ($ZBTB16^{+/-}$) where one allele of the *ZBTB16* locus is wild type and in the other exon 2 is excised. A full knockout (KO) of exon 2 in both alleles was not viable at the iPSC stage. We then treated $ZBTB16^{+/+}$ (CRISPR control No.1 iPSCs) and $ZBTB16^{+/-}$ at day 43 hCOs with 100 nM dex for 7 days and analyzed ZBTB16 protein expression, as well as the relative abundance of progenitor subtypes, with FCa and immunofluorescence at day 50 (Figure 4A).

$ZBTB16^{+/-}$ hCOs showed a significantly smaller increase of the ZBTB16 protein following dex treatment when compared with $ZBTB16^{+/+}$ hCOs (a 46% less increase; Figures 4B and 4C). FCa of the $ZBTB16^{+/+}$ hCOs validated the increase of $PAX6^+EOMES^+$ BPs under dex treatment (Figures 4D and 4E), a 22.2% increase, similar to the No.1 wild-type hCOs (Figures S2B and S2C). However, in the $ZBTB16^{+/-}$ hCOs, the number of double-positive BPs was not significantly increased by dex (Figures 4F and 4G; a 6% non-significant increase). This was further validated with immunofluorescence, where dex significantly increased the numbers of $PAX6^+EOMES^+$ BPs in $ZBTB16^{+/+}$, but not in $ZBTB16^{+/-}$, hCOs (Figure S5). Together, these results indicate that ZBTB16 is not only sufficient but also necessary for the effects of GCs on $PAX6^+EOMES^+$ BPs.

Heterochronic ZBTB16 expression in mouse fetal brain is sufficient to induce basal progenitors typically enriched in gyrified species and increase neurogenesis

Although the principles of neurogenesis are similar among all mammalian species, differences exist with respect to their temporal progression and to the abundance of progenitor subtypes populating the SVZ, which play a key role in the overall neurogenic potential. In lissencephalic species, BPs double positive for PAX6 and EOMES are very rare,[19] the neurogenic period is much shorter[32] (9 days in mice compared with 110 days in humans), and ZBTB16 is not physiologically expressed at any point during neurogenesis (Figures S3C and S3D). To analyze

Figure 3. ZBTB16 increases $PAX6^+EOMES^+$ basal progenitors in hCOs

(A) Schematic of HPS0076-derived hCO electroporations and analysis workflow.

(B) Representative images of day 50 hCOs at control and ZBTB16 OE conditions stained for Ki-67, GFP, and DAPI. Arrows indicate GFP cells that express Ki-67. (B′ and B″) Zoomed-in images of the areas.

(C) Quantification of the total number of GFP cells that are Ki-67^+.

(D) Representative images of day 50 hCOs at control and ZBTB16 OE conditions stained for PAX6, EOMES, GFP, and DAPI. Arrows indicate GFP cells that co-express PAX6 and EOMES. (D′ and D″) Zoomed-in images of the areas.

(E) Quantification of total GFP cells in each progenitor subtype.

(F) Quantification of GFP cells in different progenitor subtypes in each bin and condition normalized by GFP cells of each bin.

hCOs, human cerebral organoids; OE, overexpression; IF, immunofluorescence. For (C), significance was tested with two-tailed Mann-Whitney comparison between ZBTB16 overexpression and control plasmid. For (E) and (F), significance was tested with two-way ANOVA with Benjamini, Krieger, and Yekutieli multiple testing correction (E: p.interaction = 0.0069, F: p.interaction = 0.0002). Box and whisker plots represent 25^{th} to 75^{th} percentile of the data with the center line representing the median and whiskers representing minima and maxima. Mann-Whitney p values for (C) or post hoc p values for (E) and (F): $^{****}p \leq 0.0001$, $^{**}p \leq 0.01$, $^{*}p \leq 0.05$, ns $p > 0.05$. Scale bars, 50 μm.

See also Figure S4.

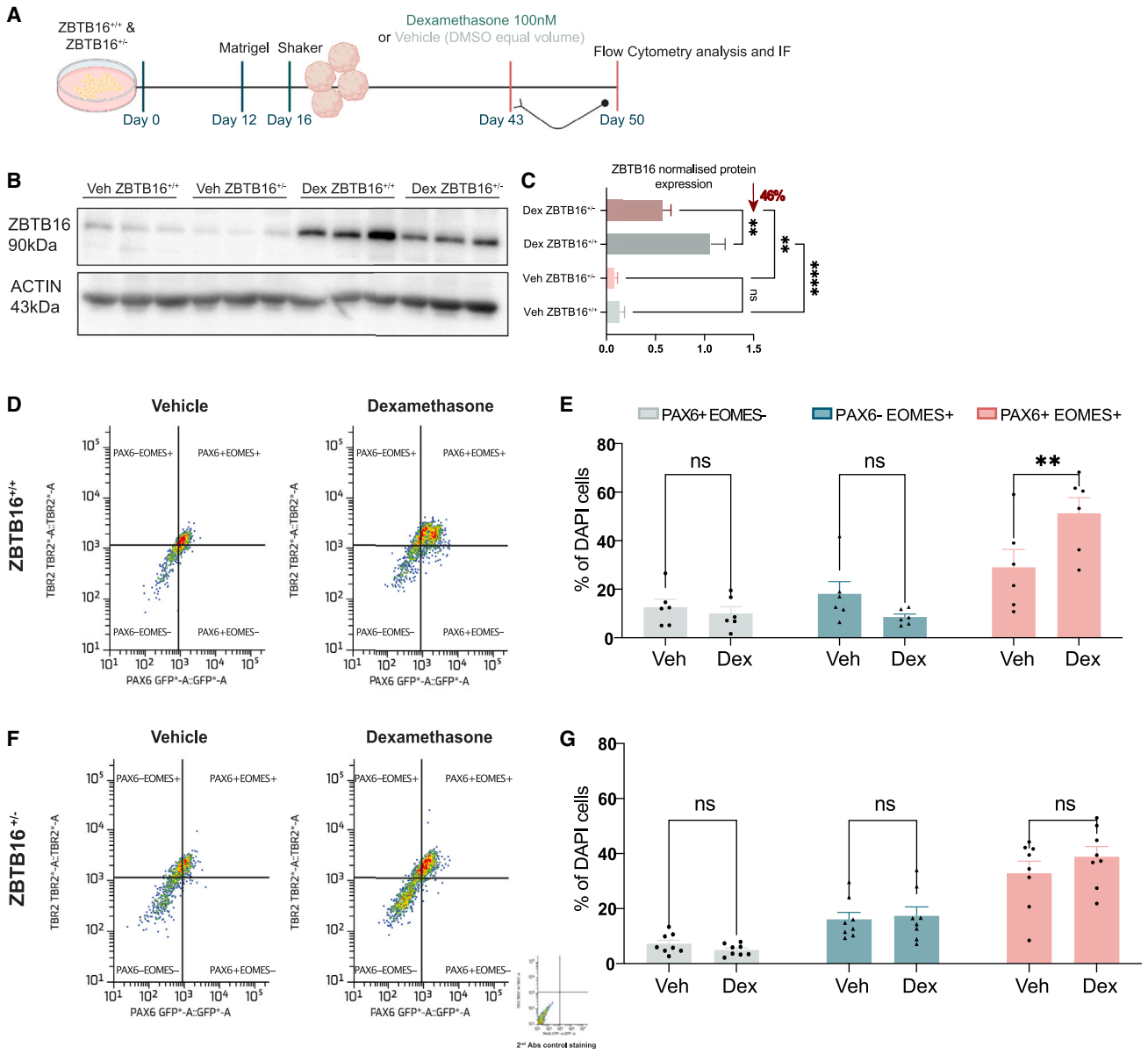

Figure 4. ZBTB16 is necessary for the effects of glucocorticoids on PAX6$^+$EOMES$^+$ basal progenitors

(A) Treatment and analysis workflow in hCOs derived from edited No.1 iPSCs with either ZBTB16$^{+/+}$ or ZBTB16$^{+/-}$ genotypes.

(B) Western blots for ZBTB16 and ACTIN in ZBTB16$^{+/+}$- or ZBTB16$^{+/-}$-derived hCOs at veh and dex. Each lane contains protein from a pool of three organoids.

(C) Quantification of western blot results.

(D) Representative images of FCa of ZBTB16$^{+/+}$-derived hCOs per treatment condition. TBR2 is an alternative name for EOMES.

(E) Quantification of the FCa results.

(F) Representative images of FCa of ZBTB16$^{+/-}$-derived hCOs per treatment condition.

(G) Quantification of the FCa results.

DMSO, dimethyl sulfoxide; hCOs, human cerebral organoids; Veh, vehicle; Dex, dexamethasone; FCa, flow cytometry analysis. For (C), (E), and (G), significance was tested with two-way ANOVA with Benjamini, Krieger, and Yekutieli multiple testing correction (C: p.interaction = 0.03, E: p.interaction = 0.0068, G: p.interaction = 0.97). Data are represented as mean ± SEM. Post hoc p values: **p $\leq$ 0.01, ns p > 0.05.

See also Figure S5 and Table S5.

whether altered expression of ZBTB16 during neurogenesis would lead to increased numbers of PAX6$^+$EOMES$^+$ BPs also in lissencephalic species, we performed *in utero* electroporations (IUEs) in mouse embryos at E13.5 with the same plasmids as for the hCOs and analyzed the effects at E16.5 (Figure 5A). Considering the more complex cellular architecture of the

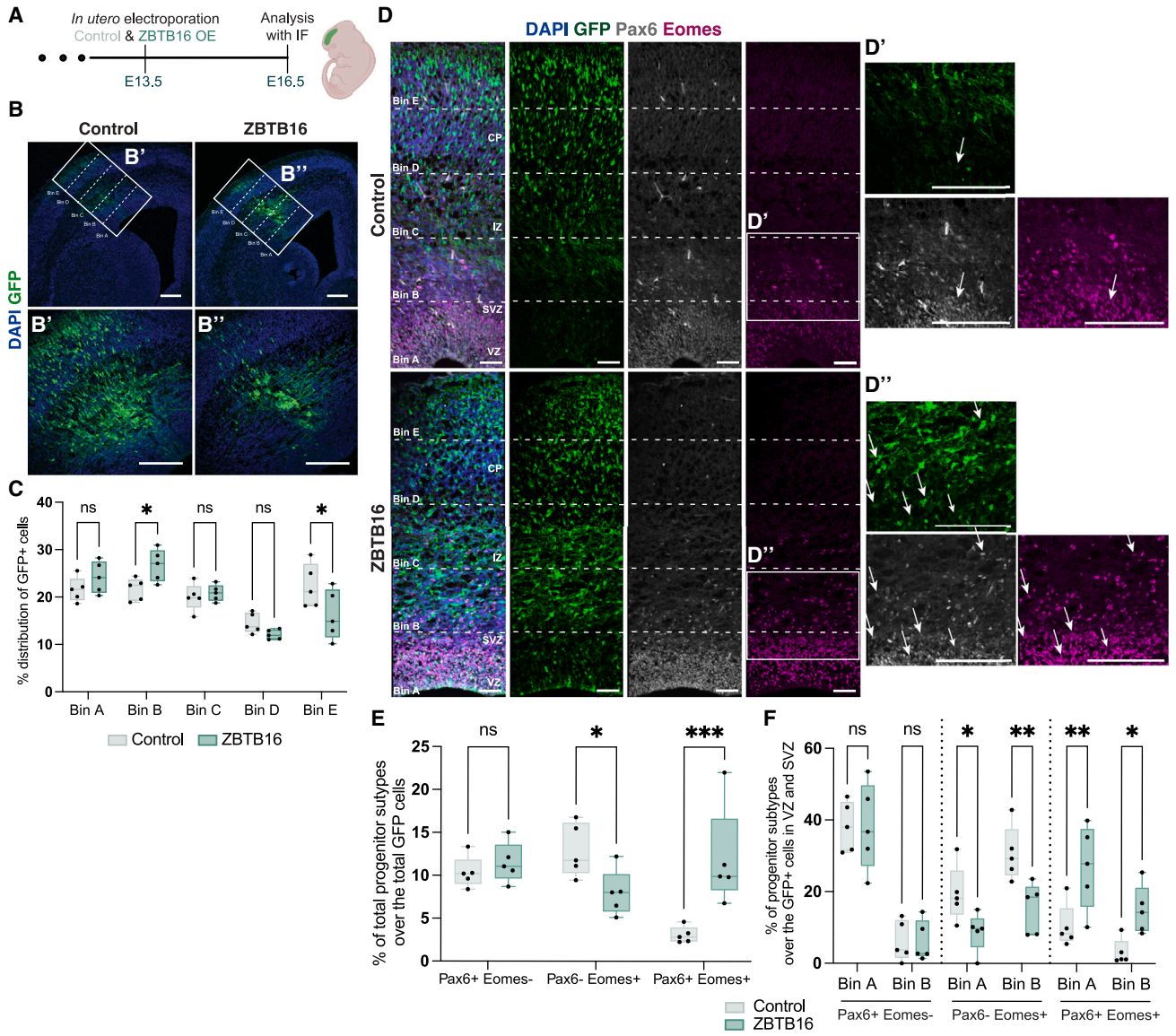

Figure 5. ZBTB16 increases PAX6$^+$EOMES$^+$ basal progenitors and neurons in a lissencephalic species

(A) Workflow of *in utero* electroporations of ZBTB16 in fetal mice.

(B) Representative images of E16.5 fetal mouse brains at control and ZBTB16 OE conditions stained for GFP and DAPI. Box indicates the electroporated areas. (B′) and (B″) are zoomed-in images of the areas.

(C) Quantification of the distribution of GFP cells in each bin normalized by the total number of GFP cells.

(D) Representative images of E16.5 fetal mouse brains at control and ZBTB16 OE conditions stained for Pax6, Eomes, GFP, and DAPI. (D′) and (D″) are zoomed-in images of the areas. Arrows indicate GFP cells that co-express Pax6 and Eomes.

(E) Quantification of GFP cells belonging in the different progenitor subtypes.

(F) Quantification of GFP cells belonging in the different progenitor subtypes in each bin normalized by GFP cells of each bin.

VZ, ventricular zone; SVZ, subventricular zone; IZ, intermediate zone; CP, cortical-like plate. For (C), (E), and (F), significance was tested with two-way ANOVA with Benjamini, Krieger, and Yekutieli multiple testing correction (C: p.interaction = 0.003, E: p.interaction = 0.0003, F: p.interaction < 0.0001). Box and whisker plots represent 25th to 75th percentile of the data with the center line representing the median and whiskers representing minima and maxima. Post hoc p values for (C), (E), and (F): ***p $\leq$ 0.001, **p $\leq$ 0.01, *p $\leq$ 0.05, ns p > 0.05. Scale bars, 50 μm.

See also Figure S6.

mouse cortex, we divided the electroporated area into five bins of equal height, where bin A includes the VZ and the SVZ; bin B, the SVZ and intermediate zone (IZ); bin C, the IZ; and bins D and E, the CP.

In mice, ZBTB16 overexpression significantly changed the distribution of the GFP$^+$ cells. ZBTB16$^+$GFP$^+$ cells accumulated in bin B with fewer cells reaching the outermost part of the CP (Figures 5B and 5C), indicating possible identity changes and/or

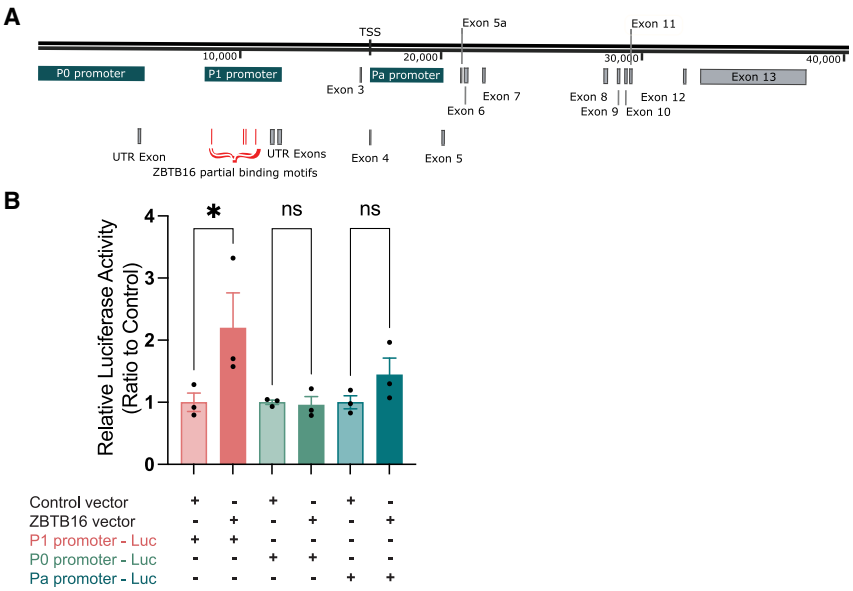

Figure 6. ZBTB16 activates a PAX6 promoter

(A) Schematic representation of the human *PAX6* locus.

(B) Quantification of the luciferase reporter assay results per promoter region and vector. Results are normalized to control transfections. Significance was tested with two-way ANOVA with Benjamini, Krieger, and Yekutieli multiple testing correction ($p = 0.04$). Data are represented as mean ± SEM. Post hoc p values: *$p \leq 0.05$, ns $p > 0.05$.

altered timing of differentiation. Similar to hCOs, we found more Pax6$^+$Eomes$^+$ BPs (Figures 5D and 5E; a 8.8% overall increase) in bins A and B (Figure 5F; 16.5% and 11.8%, respectively). Interestingly, in mice, Pax6$^-$Eomes$^+$ IPs, which represent the vast majority of endogenous BPs of lissencephalic species,[19] were significantly decreased after ZBTB16 overexpression (Figures 5E and 5F; a 10.6% decrease in bin A and a 15.1% decrease in bin B), indicating a cell-type shift upon ZBTB16 overexpression. To dissect the proliferation capacity for cells expressing ZBTB16, we performed cell-cycle re-entry analysis in mice, as cell-cycle dynamics are well known for this species. Mice electroporated at E13.5 with a control or ZBTB16-overexpressing plasmid received a BrdU injection at E15.5, 24 h before they were sacrificed at E16.5. We then stained for Ki67, BrdU, and GFP and quantified the proportion of BrdU$^+$GFP$^+$ cells that are also Ki67$^+$ to label cells that re-entered the cell cycle. Indeed, we find more BrdU$^+$Ki67$^+$GFP$^+$ cells (as a fraction of BrdU$^+$GFP$^+$) in bins A and B, the same bins where we find the increase in Pax6$^+$Eomes$^+$ cells, after ZBTB16 overexpression (Figures S6A and S6B). This indicates that ZBTB16 prompts the cells to re-enter the cell cycle. Our results suggest that ZBTB16 overexpression during lissencephalic neurogenesis leads to more gyrified species-enriched BPs and increased self-renewing capacity at the expense of the endogenous neurogenic progenitors.

To further study what this means for neurogenesis, we analyzed the neuronal output. Here, we found that ZBTB16 overexpression led to increased numbers of deep-layer Bcl11b$^+$ (a 33.3% significant increase) and Tbr1$^+$ (a 4.3% significant increase; Figures S6C and S6D) neurons but not of upper-layer Satb2$^+$ neurons (Figures S6F and S6G). Given that, in mice, neurons are generated in sequential waves with upper-layer neurons being born mainly starting at E14.5 and not before,[33] we repeated the same experiments but performing the IUEs a day later, at E14.5, and analyzed the neuronal output at E17.5. Indeed, at this developmental stage, ZBTB16 overexpression led to increased numbers of Satb2$^+$ cells (a 14% significant increase; Figures S6I and S6J), as well as of Bcl11b$^+$ cells (a 26% significant increase; Figure S6J). When examining the distribution of neurons, we found an accumulation in the SVZ and IZ areas with fewer neurons having reached the CP after ZBTB16 overexpression (Figures S6E and S6H). This supports that the higher proliferative capacity of the PAX6$^+$ EOMES$^+$ BPs associates with a potentially longer neurogenic period similar to the effects of dex in hCOs. In fact, when analyzing the distribution of neurons across the five bins 6 days, but not 3 days, post electroporation at postnatal day 0, there were no significant differences with ZBTB16 overexpression (Figures S6K–S6O), indicating that migratory processes are probably not affected.

ZBTB16 directly induces PAX6 expression

Considering that dex seems to sustain PAX6 expression in EOMES$^+$ cells via ZBTB16, even in a lissencephalic species where they are physiologically mutually exclusive,[34–36] and that ZBTB16 is a TF, we analyzed the activation capacity of ZBTB16 on *PAX6* human promoters. *PAX6* has three promoter regions that regulate tissue-specific expression and are highly conserved between humans and rodents: the P0, P1, and Pa promoters[37,38] (Figure 6A). Using luciferase assays, we found that ZBTB16 activates the P1 promoter of *PAX6* but not the P0 and Pa promoters (Figure 6B). This suggests that ZBTB16 could regulate PAX6 expression via the P1 promoter, which is active during neocortical development, in comparison with the P0 and Pa promoters, which are minimally active.[37] This could be a potential mechanism responsible for sustaining Pax6 expression in Eomes$^+$ cells even in mice, whereby ZBTB16 overexpression circumvents the negative feedback loop that physiologically ensures that Pax6 and Eomes are not co-expressed in rodents.[34–36]

GCs interact with the *ZBTB16* genetic and epigenetic landscape

To analyze the mechanisms via which the physiological temporal expression pattern of ZBTB16 is affected by GCs, we investigated the gene regulatory landscape of the human *ZBTB16* locus in response to GCs. ENCODE data indicate the existence of intronic GR response elements (GREs) at the human *ZBTB16* locus (Figure 7A). We have previously shown that activation of GR leads to DNA methylation changes in GREs of target genes associating with changes in gene transcription.[39,40] To identify the specific enhancers by which GR induces *ZBTB16*

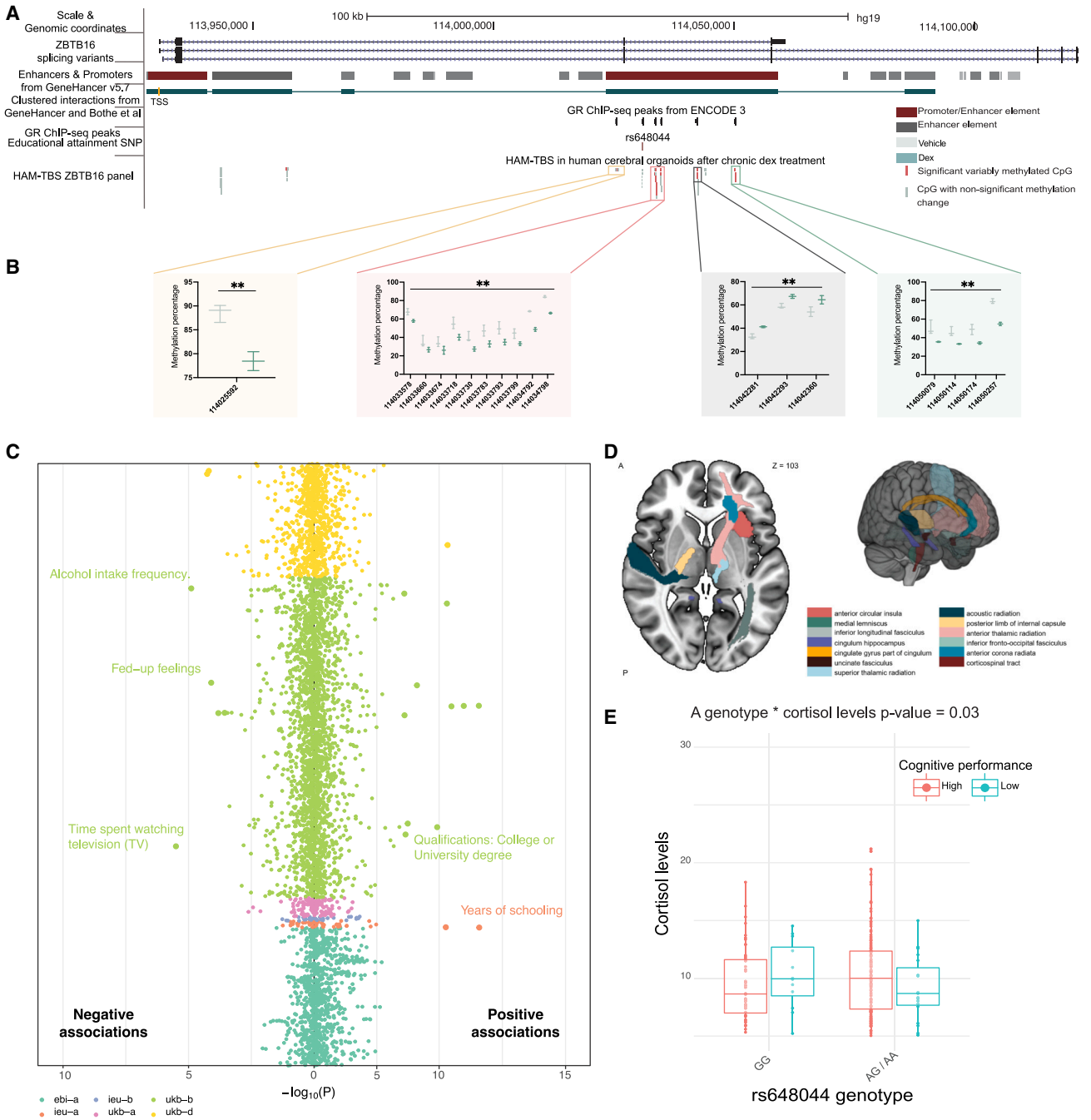

Figure 7. Glucocorticoids interact with the genetic and epigenetic landscape of *ZBTB16* to impact postnatal neurobehavioral and structural phenotypes

(A) Graphical representation of the *ZBTB16* locus including the position of the amplicons for HAM-TBS and pyrosequencing.

(B) HAM-TBS results for CpGs with significantly altered DNA methylation levels following exposure of hCOs to 7 days of 100 nM dex vs. veh.

(C) Plot depicting MRa-PheWAS associations, as log-p value, for rs648044 with various phenotypes from the UK Biobank. Single phenotypes are depicted as individual points. Associations are presented based on negative (negative MRa estimate, i.e., lower quantitative measures with A allele effects) or positive (positive MRa estimate, i.e., higher quantitative measures with A allele effects) effects. Color coding reflects the different sources of GWASs depicted in the legend. Traits that remain significant following Benjamini-Hochberg correction are shown with larger dots and are listed in Table S7. Specific neurobehavioral traits are labeled.

(D) Illustration of significant MRa associations of rs648044 with brain imaging phenotypes mapped onto brain atlases. See also Table S7.

(E) Cortisol levels before GW28 according to rs648044 genotype and cognitive performance as assessed using the Bayley-III cognitive subscale in the data from the ITU (InTraUterine) cohort.

(legend continued on next page)

expression, we treated day 30 hCOs with 100 nM dex for 7 days and used highly accurate method for targeted bisulfite sequencing[41] (HAM-TBS) and pyrosequencing to measure DNA methylation of all GREs, as identified by public GR-chromatin immunoprecipitation sequencing datasets, and additional non-GR-related regulatory elements (Figure 7A). Out of 55 CpGs covered with HAM-TBS and 8 covered with pyrosequencing, 44 were located within GREs and 19 in enhancer elements lacking GR-binding sites. Although only 1 of the CpGs outside these GR-binding regions showed significant DNA methylation changes following dex stimulation, this was true for 18 of the 44 CpGs around GREs (Figure 7B; Table S6). All significantly altered GRE-CpGs are located in enhancer regions that loop to the transcriptional start site of *ZBTB16* ("GeneHancer" track in Figure 7A and Bothe et al.[42]). Our data thus support a model in which GR binds to these enhancer elements as evidenced by altered DNA methylation and increases *ZBTB16* transcription.

Knowing that environmental factors, including GCs, can interact with the genetic landscape to modulate their effects on expression,[43] we next analyzed gene variants within the *ZBTB16* locus. We cataloged single-nucleotide polymorphisms (SNPs) in the *ZBTB16* locus that were previously associated with neurobehavioral and brain structural outcomes (GWAS Catalog) and identified rs648044 as the only variant associated with both. rs648044 has been associated with educational attainment in two genome-wide association studies (GWASs) for this trait (Lee et al.[44]: N = 1,131,881, FDR = 9×10^{-9}, and Okbay et al.[45]: N = 3,037,499, FDR = 2×10^{-8}) and with generalized cortical thickness[46] (N = 35,657 individuals, FDR = 6×10^{-9}). In the latter GWAS on cortical morphology, gene-level analysis also identified the whole *ZBTB16* locus to be significantly associated with generalized cortical surface area (FDR = 7.2×10^{-14}) and thickness (FDR = 1.9×10^{-8}), thus suggesting relevance of *ZBTB16* for adult cortical morphology.

In our DNA methylation assays, CpGs surrounding this SNP showed low methylation levels supporting its regulatory activity (Figure S7A; Table S6). To further explore its role in gene regulation, we first analyzed whether this SNP moderates dex-induced activity of the surrounding 200 base pair (bp) enhancer elements using a self-transcribing active regulatory region qPCR (STARR-qPCR) approach. Indeed, this region possesses enhancer activity that is increased with GR activation (Figure S7B). The extent of dex-induced activity was rs648044 allele dependent, with the allele associated with higher educational attainment (A allele), conferring a significantly stronger increase following dex (Figure S7C). Next, we used CRISPR-Cas9 to knock out 400 nucleotides surrounding rs648044 in No.1 iPSCs to identify whether this enhancer affects *ZBTB16* transcription in hCOs. The rs648044 genotype of No.1 iPSCs is heterozygous (G/A), with the rarer A allele (allele frequency = 0.35) creating a degenerated partial GR-binding site (described half site[47]: AGXACAG, rs648044 creates: AGC[A/G]GAG). A KO of the A allele resulted in rs648044$^{G/-}$ cells that only carry the G allele (Figure S7D). Using the edited cell line (rs648044$^{G/-}$) and the control cell line carrying both alleles (rs648044$^{G/A}$), we found that the absence of the A allele confers significantly smaller induction of *ZBTB16* following 100 nM dex in day 30 hCOs treated for 7 days (Figures S7E and S7F), suggesting that the enhancer containing rs648044 modulates dex-mediated transcriptional effects on *ZBTB16*.

GCs × rs648044 effects on *ZBTB16* relate to beneficial postnatal outcomes

Given the functional effects of rs648044 on GC-induced ZBTB16 expression, we used Mendelian randomization analysis at the phenome-wide level (MRa-PheWAS) to identify causal effects of *ZBTB16* levels on 7,323 phenotypes from the UK Biobank and the NHGRI-EBI GWAS Catalog that include, among many others, neurobehavioral traits and adult neuroimaging data (Table S7). We used rs648044 as exposure and the magnitude of the allele-specific enhancer activity changes following dex in the STARR-qPCR experiment as instrument to test for these associations. MRa-PheWAS provided strong evidence for associations with multiple outcomes as indicated by the QQ plot (Figure S7G). MRa on various phenotypes, including endophenotypes and diseases (N = 4,360), showed significant associations of GC-altered *ZBTB16* expression with 22 phenotypes after multiple testing correction. These included associations of enhanced GC-induced *ZBTB16* activity with years of schooling and whether individuals had obtained a college or university degree (Figure 7C; Table S7), both direct measures of educational attainment. The allele with less induced activity was associated with "fed-up feelings," a phenotype related to neuroticism,[48] "alcohol intake," and "time spent watching television" (Figure 7C), suggesting associations of higher dex-induced *ZBTB16* levels with beneficial postnatal outcomes. Given the previously published relationships of both educational attainment[49–52] and rs648044[44–46] with cortical volumes and white matter measures, we also ran an MRa-PheWAS on all neuroimaging phenotypes (N = 3,143) in the UK Biobank using the same instrument. We observed 21 significant associations after multiple testing correction (Figures 7D and S7H; Table S7), with the majority related to altered white matter measures and with higher anterior circular insula thickness (Figure 7D).

To further examine the importance of GC-altered *ZBTB16* levels during neurogenesis for postnatal phenotypes, we used data from the InTraUterine sampling in early pregnancy (ITU) prospective cohort study[53] to test the association of the rs648044 A allele and prenatal maternal cortisol with cognitive performance. We defined neurodevelopmental cognitive delay, using the Bayley cognitive subscale, as 1 standard deviation (SD) below the sample mean (Figure S7I). For children testing below and above 1 SD of cognitive performance, a complete set of salivary cortisol

GR, glucocorticoid receptor; ChIP, chromatin immunoprecipitation; Seq, sequencing; SNP, single-nucleotide polymorphism; HAM-TBS, highly accurate method for targeted bisulfite sequencing; Dex, dexamethasone; veh, vehicle; MRa, Mendelian randomization analysis; Phe-WAS, phenome-wide association study. For (B), significance was tested with two-way ANOVA with Benjamini, Krieger, and Yekutieli multiple testing correction. For (E), significance was tested with a logarithmic regression. Box and whisker plots represent 25th to 75th percentile of the data with the center line representing the median and whiskers representing minima and maxima. Post hoc p values: **$p \leq 0.01$.
See also Figure S7 and Tables S6 and S7.

data during pregnancy and fetal genotypes was available for 246 mother-child dyads before GW28 and for 221 mother-child dyads after GW28 (Table S7). Using logistic regressions, we tested the interaction of rs648044 A allele × mean cortisol levels before GW28, after GW28, or across pregnancy on cognitive performance at 3 years of age (see STAR Methods for covariates). The interaction was not significantly associated with cognitive performance when using maternal cortisol levels from across pregnancy (p value = 0.055). When stratifying the data for cortisol levels before GW28 and, thus, during neurogenesis, the interaction of rs648044 A allele with cortisol was significantly associated with higher cognitive performance (p value = 0.035; Figure 7E), an effect not found with cortisol data after GW28 (p value = 0.46; Table S7), i.e., after completion of cortical neurogenesis.

Thus, higher GC-induced *ZBTB16* expression in rs648044 A allele carriers during neurogenesis is associated with higher cognitive performance and educational attainment, lower neuroticism measures, and increased cortical thickness as well as altered white matter measures postnatally. This suggests that the genetic association of this variant with postnatal neurobehavioral and structural measures found in the literature could be mediated in part by its effects on GC-induced *ZBTB16* levels in early brain development and in consequence their effects on neurogenesis.

DISCUSSION

Precise temporal and spatial regulation of gene expression by TFs is key for the proper unfolding of neurogenic processes.[25] ZBTB16 exhibits species-specific expression patterns during development. In lissencephalic species, like rodents, Zbtb16 is not expressed during cortical neurogenesis,[29] whereas in humans, it is expressed at early stages of neurogenesis, suggesting divergent actions between species (Figures S3C–S3E). GCs, by sustaining the expression of ZBTB16 during the neurogenic period, when it is not present physiologically, result in increased numbers of $Pax6^{+}Eomes^{+}$ progenitors, indicating their role in enhancing gyrified species-enriched neurogenic processes. GCs can thus extend or open a sensitive developmental time window for production of gyrencephalic-enriched BPs, even in a lissencephalic species, via the action of ZBTB16, resulting in enhanced neurogenic potential. ZBTB16 seems to specifically mediate GC effects on neurogenesis since it is differentially regulated only in progenitor cells, as seen with our single-cell data. It is unlikely that it would mediate other GC effects reported in the literature related to neuronal function.[54,55]

Given the high prevalence of premature births, GC excess during human neurodevelopment through administration of sGCs is a very common phenomenon.[11] In fact, in ~615,000 extreme preterm pregnancies per year, sGC treatments, if used, would take place in a period of active neurogenesis, before GW28.[11,14] It was recently shown that sGCs given at GW22 increase the survival rate of the offspring 3.5 times.[9] While endogenous GCs are vital for fetal organ maturation,[4] prenatal GC excess has been extensively associated with long-term metabolic, endocrine, and cardiovascular problems[2] and risk for neurodevelopmental[56] and mental[57] disorders in the offspring. Evidence from a recent meta-analysis of studies including more than 1.25 million children re-affirms the association of sGC exposure with negative effects on cognitive and neuropsychiatric outcomes when administered to children with late-preterm or term birth. However, the authors also report a significantly lower risk for neurodevelopmental impairments in children with extremely preterm birth (<GW28) that were treated with sGCs between GW22 and GW27.[12] This meta-analysis could point to potential differential effects of GCs on neurodevelopmental outcomes depending on the developmental time window they were administered in.

One process that is different among extremely preterm and term or adult brains and might contribute to these dichotomous effects is cortical neurogenesis, which peaks at ~GW20 and is reduced but present until GW28 in the SVZ of the brain.[14] This suggests that extremely preterm-born children are still treated within the time window of active cortical neurogenesis. Such differential effects are supported by a study in mice in which dex administration during neurogenesis was associated with anxiolytic and anti-depressive-like behavior in the adult offspring,[58] whereas increased, prolonged exposure to GCs following completion of cortical neurogenesis has repeatedly been associated with increased anxiety and depressive-like behaviors and decreased cognitive ability.[59] Our research highlights a potential molecular and cellular pathway for the lasting effects of prenatal GC exposure during neurogenesis with *ZBTB16* as a critical mediator. Nevertheless, the association with postnatal behavioral and structural outcomes should be interpreted with caution as the increased number of neurons may ultimately not contribute to brain function postnatally.

In conclusion, our work provides a molecular and cellular explanation for how GC exposure during neurogenesis influences cortical cytoarchitecture. It underscores the significance of GCs in human neurogenic processes and suggests a pathway to understand the benefits of early sGC use on behavioral and neurodevelopmental measures. This insight can help refine treatment guidelines based on the timing of sGC administration during pregnancy.

STAR★METHODS

Detailed methods are provided in the online version of this paper and include the following:

- KEY RESOURCES TABLE
- RESOURCE AVAILABILITY
  - Lead contact
  - Materials availability
  - Data and code availability
- EXPERIMENTAL MODEL AND STUDY PARTICIPANT DETAILS
  - Cell lines
  - Cerebral organoids
  - Mice
- METHOD DETAILS
  - *In utero* electroporations of mice
  - Electroporations of human cerebral organoids
  - Glucocorticoid treatment in cerebral organoids and mice

- Immunofluorescence
- Protein isolation and western blot
- RNA isolation and quantitative PCR
- Plasmids preparation
- Luciferase reporter assays
- CRISPR-Cas9 editions of hiPSCs
- Flow cytometry
- Targeted bisulfite sequencing
- Methylation analysis by bisulfite pyrosequencing
- Bulk RNA sequencing
- HPS0076 chronic single-cell dataset
- No.1 single-cell dataset
- STARR (Self-Transcribing Active Regulatory Region sequencing)-qPCR
- Mendelian randomization analysis (Mra) and Phenome-wide association (PheWAS) study
- InTraUterine prospective pregnancy cohort study

● QUANTIFICATION AND STATISTICAL ANALYSIS

- Image analysis and quantifications
- Statistics & plots

SUPPLEMENTAL INFORMATION

Supplemental information can be found online at https://doi.org/10.1016/j.neuron.2024.02.005.

ACKNOWLEDGMENTS

L.D. acknowledges support by the Joachim Herz Foundation. We thank Mira Erhart, Dr. Michael Czisch, and Dr. Benoit Boulat for informative discussions on brain structural measures. We thank Nathalie Gerstner and Dr. Janine Knauer-Arloth for discussion on analysis. We thank Dr. Nadine Gogolla for discussion on the broader relevance of the findings. This work was supported by the Hope for Depression Research Foundation and a NARSAD Distinguished Investigator award to E.B.B.

AUTHOR CONTRIBUTIONS

Conceptualization, A.C.K., C.C., and E.B.B.; methodology, A.C.K. and C.K.; software, L.D., N.K., D.P., S.R., A.S., D.C., M.L.P., S.S., E.W., and K.H.; validation, M.H.L. and C.R.; formal analysis, L.D., N.K., A.S., and D.C.; investigation, A.C.K., C.C., C.K., M.H.L., C.R., V.S., B.W., M.K., M.L., and S.S.; resources, D.C., M.L.P., S.S., E.W., K.H., K.R., S.P.G., and M.R.H.; data curation, A.C.K., L.D., and S.R.; writing – original draft, A.C.K. and E.B.B.; writing – review & editing, A.C.K., C.C., C.K., L.D., N.K., D.P., S.P.G., M.L., S.C., and E.B.B.; visualization, A.C.K.; supervision, A.C.K., C.C., C.K., S.C., and E.B.B.; project administration, A.C.K. and E.B.B.; and funding acquisition, E.B.B.

DECLARATION OF INTERESTS

The authors declare no competing interests.

Received: January 17, 2023
Revised: August 15, 2023
Accepted: February 6, 2024
Published: March 4, 2024

REFERENCES

1. Barker, D.J.P. (2004). The developmental origins of chronic adult disease. Acta Paediatr. Suppl. *93*, 26–33. https://doi.org/10.1080/08035320410022730.

2. Monk, C., Lugo-Candelas, C., and Trumpff, C. (2019). Prenatal Developmental Origins of Future Psychopathology: Mechanisms and Pathways. Annu. Rev. Clin. Psychol. *15*, 317–344. https://doi.org/10.1146/annurev-clinpsy-050718-095539.

3. Krontira, A.C., Cruceanu, C., and Binder, E.B. (2020). Glucocorticoids as Mediators of Adverse Outcomes of Prenatal Stress. Trends Neurosci. *43*, 394–405. https://doi.org/10.1016/j.tins.2020.03.008.

4. Carson, R., Monaghan-Nichols, A.P., DeFranco, D.B., and Rudine, A.C. (2016). Effects of antenatal glucocorticoids on the developing brain. Steroids *114*, 25–32. https://doi.org/10.1016/j.steroids.2016.05.012.

5. Edwards, P.D., and Boonstra, R. (2018). Glucocorticoids and CBG during pregnancy in mammals: diversity, pattern, and function. Gen. Comp. Endocrinol. *259*, 122–130. https://doi.org/10.1016/j.ygcen.2017.11.012.

6. Harris, A., and Seckl, J. (2011). Glucocorticoids, prenatal stress and the programming of disease. Hormones Behav. *59*, 279–289. https://doi.org/10.1016/j.yhbeh.2010.06.007.

7. Lajic, S., Karlsson, L., and Nordenström, A. (2018). Prenatal Treatment of Congenital Adrenal Hyperplasia: Long-Term Effects of Excess Glucocorticoid Exposure. Horm. Res. Paediatr. *89*, 362–371. https://doi.org/10.1159/000485100.

8. Committee on Obstetric Practice (2017). Antenatal Corticosteroid Therapy for Fetal Maturation. Obstet. Gynecol. *130*, e102–e109. https://doi.org/10.1097/AOG.0000000000002237.

9. Vidavalur, R., Hussain, Z., and Naveed, H. (2022). Association of Survival at 22 Weeks' Gestation With Use of Antenatal Corticosteroids and Mode of Delivery in the United States. JAMA Pediatr. *177*, 90–93.

10. Cao, G., Liu, J., and Liu, M. (2022). Global, Regional, and National Incidence and Mortality of Neonatal Preterm Birth, 1990–2019. JAMA Pediatr. *176*, 787–796. https://doi.org/10.1001/jamapediatrics.2022.1622.

11. Chawanpaiboon, S., Vogel, J.P., Moller, A.B., Lumbiganon, P., Petzold, M., Hogan, D., Landoulsi, S., Jampathong, N., Kongwattanakul, K., Laopaiboon, M., et al. (2019). Global, regional, and national estimates of levels of preterm birth in 2014: a systematic review and modelling analysis. Lancet Glob. Health *7*, e37–e46. https://doi.org/10.1016/S2214-109X(18)30451-0.

12. Ninan, K., Liyanage, S.K., Murphy, K.E., Asztalos, E.V., and McDonald, S.D. (2022). Evaluation of Long-term Outcomes Associated With Preterm Exposure to Antenatal Corticosteroids: A Systematic Review and Meta-analysis. JAMA Pediatr. *176*, e220483. https://doi.org/10.1001/jamapediatrics.2022.0483.

13. Mcewen, B.S., Bowles, N.P., Gray, J.D., Hill, M.N., Hunter, R.G., Karatsoreos, I.N., and Nasca, C. (2015). Mechanisms of stress in the brain. Nat. Neurosci. *18*, 1353–1363. https://doi.org/10.1038/nn.4086.

14. Malik, S., Vinukonda, G., Vose, L.R., Diamond, D., Bhimavarapu, B.B.R., Hu, F., Zia, M.T., Hevner, R., Zecevic, N., and Ballabh, P. (2013). Neurogenesis continues in the third trimester of pregnancy and is suppressed by premature birth. J. Neurosci. *33*, 411–423. https://doi.org/10.1523/JNEUROSCI.4445-12.2013.

15. Lancaster, M.A., and Knoblich, J.A. (2014). Generation of cerebral organoids from human pluripotent stem cells. Nat. Protoc. *9*, 2329–2340. https://doi.org/10.1038/nprot.2014.158.

16. Cruceanu, C., Dony, L., Krontira, A.C., Fischer, D.S., Roeh, S., Di Giaimo, R., Kyrousi, C., Kaspar, L., Arloth, J., Czamara, D., et al. (2022). Cell-Type-Specific Impact of Glucocorticoid Receptor Activation on the Developing Brain: A Cerebral Organoid Study. Am. J. Psychiatry *179*, 375–387. https://doi.org/10.1176/appi.ajp.2021.21010095.

17. Prasad, R., Jung, H., Tan, A., Song, Y., Moon, S., Shaker, M.R., Sun, W., Lee, J., Ryu, H., Lim, H.K., et al. (2021). Hypermethylation of Mest promoter causes aberrant Wnt signaling in patients with Alzheimer's disease. Sci. Rep. *11*, 20075. https://doi.org/10.1038/s41598-021-99562-9.

18. Zhang, M., Haughey, M., Wang, N.Y., Blease, K., Kapoun, A.M., Couto, S., Belka, I., Hoey, T., Groza, M., Hartke, J., et al. (2020). Targeting the Wnt signaling pathway through R-spondin 3 identifies an anti-fibrosis

treatment strategy for multiple organs. PLoS One *15*, e0229445. https://doi.org/10.1371/journal.pone.0229445.

19. Dehay, C., Kennedy, H., and Kosik, K.S. (2015). The Outer Subventricular Zone and Primate-Specific Cortical Complexification. Neuron *85*, 683–694. https://doi.org/10.1016/j.neuron.2014.12.060.
20. Betizeau, M., Cortay, V., Patti, D., Pfister, S., Gautier, E., Bellemin-Ménard, A., Afanassieff, M., Huissoud, C., Douglas, R.J., Kennedy, H., et al. (2013). Precursor Diversity and Complexity of Lineage Relationships in the Outer Subventricular Zone of the Primate. Neuron *80*, 442–457. https://doi.org/10.1016/j.neuron.2013.09.032.
21. de Juan Romero, C., Bruder, C., Tomasello, U., Sanz-Anquela, J.M., and Borrell, V. (2015). Discrete domains of gene expression in germinal layers distinguish the development of gyrencephaly. EMBO J. *34*, 1859–1874. https://doi.org/10.15252/embj.201591176.
22. Florio, M., and Huttner, W.B. (2014). Neural progenitors, neurogenesis and the evolution of the neocortex. Development *141*, 2182–2194. https://doi.org/10.1242/dev.090571.
23. Matsumoto, N., Tanaka, S., Horiike, T., Shinmyo, Y., and Kawasaki, H. (2020). A discrete subtype of neural progenitor crucial for cortical folding in the gyrencephalic mammalian brain. eLife *9*, 1–26. https://doi.org/10.7554/eLife.54873.
24. Borrell, V., and Götz, M. (2014). Role of radial glial cells in cerebral cortex folding. Curr. Opin. Neurobiol. *27*, 39–46. https://doi.org/10.1016/j.conb.2014.02.007.
25. Silbereis, J.C., Pochareddy, S., Zhu, Y., Li, M., and Sestan, N. (2016). The Cellular and Molecular Landscapes of the Developing Human Central Nervous System. Neuron *89*, 248–268. https://doi.org/10.1016/j.neuron.2015.12.008.
26. Xiong, Y., Zhang, Y., Xiong, S., and Williams-Villalobo, A.E. (2020). A glance of p53 functions in brain development, neural stem cells, and brain cancer. Biology *9*, 1–13. https://doi.org/10.3390/biology9090285.
27. Djuric, U., Rodrigues, D.C., Batruch, I., Ellis, J., Shannon, P., and Diamandis, P. (2017). Spatiotemporal proteomic profiling of human cerebral development. Mol. Cell. Proteomics *16*, 1548–1562. https://doi.org/10.1074/mcp.M116.066274.
28. Liu, T.M., Lee, E.H., Lim, B., and Shyh-Chang, N. (2016). Concise Review: Balancing Stem Cell Self-renewal and Differentiation with PLZF. Stem Cells *34*, 277–287. https://doi.org/10.1002/stem.2270.
29. Avantaggiato, V., Pandolfi, P.P., Ruthardt, M., Hawe, N., Acampora, D., Pelicci, P.G., and Simeone, A. (1995). Developmental analysis of murine Promyelocyte Leukemia Zinc Finger (PLZF) gene expression: implications for the neuromeric model of the forebrain organization. J. Neurosci. *15*, 4927–4942.
30. Pebworth, M.P., Ross, J., Andrews, M., Bhaduri, A., and Kriegstein, A.R. (2021). Human intermediate progenitor diversity during cortical development. Proc. Natl. Acad. Sci. USA *118*, 1–10. https://doi.org/10.1073/pnas.2019415118.
31. Hai, L., Szwarc, M.M., Lanza, D.G., Heaney, J.D., and Lydon, J.P. (2019). Using CRISPR/Cas9 engineering to generate a mouse with a conditional knockout allele for the promyelocytic leukemia zinc finger transcription factor. Genesis *57*, e23281. https://doi.org/10.1002/dvg.23281.
32. Stepien, B.K., Vaid, S., and Huttner, W.B. (2021). Length of the Neurogenic Period—A Key Determinant for the Generation of Upper-Layer Neurons During Neocortex Development and Evolution. Front. Cell Dev. Biol. *9*, 676911. https://doi.org/10.3389/fcell.2021.676911.
33. Magrinelli, E., Baumann, N., Wagener, R.J., Glangetas, C., Bellone, C., Jabaudon, D., and Klingler, E. (2022). Heterogeneous fates of simultaneously-born neurons in the cortical ventricular zone. Sci. Rep. *12*, 6022. https://doi.org/10.1038/s41598-022-09740-6.
34. Manuel, M., Georgala, P.A., Carr, C.B., Chanas, S., Kleinjan, D.A., Martynoga, B., Mason, J.O., Molinek, M., Pinson, J., Pratt, T., et al. (2007). Controlled overexpression of Pax6 in vivo negatively auto-regulates the Pax6 locus, causing cell-autonomous defects of late cortical progenitor proliferation with little effect on cortical arealization. Development *134*, 545–555. https://doi.org/10.1242/dev.02764.
35. Sansom, S.N., Griffiths, D.S., Faedo, A., Kleinjan, D.J., Ruan, Y., Smith, J., van Heyningen, V., Rubenstein, J.L., and Livesey, F.J. (2009). The level of the transcription factor Pax6 is essential for controlling the balance between neural stem cell self-renewal and neurogenesis. PLoS Genet. *5*, e1000511. https://doi.org/10.1371/journal.pgen.1000511.
36. Elsen, G.E., Bedogni, F., Hodge, R.D., Bammler, T.K., MacDonald, J.W., Lindtner, S., Rubenstein, J.L.R., and Hevner, R.F. (2018). The Epigenetic Factor Landscape of Developing Neocortex Is Regulated by Transcription Factors Pax6→Tbr2→Tbr1. Front. Neurosci. *12*, 571. https://doi.org/10.3389/fnins.2018.00571.
37. Anderson, T.R., Hedlund, E., and Carpenter, E.M. (2002). Differential Pax6 promoter activity and transcript expression during forebrain development. Mech. Dev. *114*, 171–175.
38. Tyas, D.A., Simpson, T.I., Carr, C.B., Kleinjan, D.A., Van Heyningen, V., Mason, J.O., and Price, D.J. (2006). Functional conservation of Pax6 regulatory elements in humans and mice demonstrated with a novel transgenic reporter mouse. BMC Dev. Biol. *6*, 21. https://doi.org/10.1186/1471-213X-6-21.
39. Penner-Goeke, S., Bothe, M., Rek, N., Kreitmaier, P., Pöhlchen, D., Kühnel, A., Glaser, L.V., Kaya, E., Krontira, A.C., Röh, S., et al. (2023). High-throughput screening of glucocorticoid- induced enhancer activity reveals mechanisms of stress-related psychiatric disorders. Proc. Natl. Acad. Sci. USA *120,* e2305773120. https://doi.org/10.1073/pnas.2305773120.
40. Provençal, N., Arloth, J., Cattaneo, A., Anacker, C., Cattane, N., Wiechmann, T., Röh, S., Ködel, M., Klengel, T., Czamara, D., et al. (2020). Glucocorticoid exposure during hippocampal neurogenesis primes future stress response by inducing changes in DNA methylation. Proc. Natl. Acad. Sci. USA *117*, 23280–23285. https://doi.org/10.1073/pnas.1820842116.
41. Roeh, S., Wiechmann, T., Sauer, S., Ködel, M., Binder, E.B., and Provençal, N. (2018). HAM-TBS: High-accuracy methylation measurements via targeted bisulfite sequencing. Epigenetics Chromatin *11*, 39. https://doi.org/10.1186/s13072-018-0209-x.
42. Bothe, M., Buschow, R., and Meijsing, S.H. (2021). Glucocorticoid signaling induces transcriptional memory and universally reversible chromatin changes. Life Sci. Alliance *4*, 1–17. https://doi.org/10.26508/lsa.202101080.
43. Klengel, T., and Binder, E.B. (2015). Epigenetics of Stress-Related Psychiatric Disorders and Gene × Environment Interactions. Neuron *86*, 1343–1357. https://doi.org/10.1016/j.neuron.2015.05.036.
44. Lee, J.J., Wedow, R., Okbay, A., Kong, E., Maghzian, O., Zacher, M., Nguyen-Viet, T.A., Bowers, P., Sidorenko, J., Karlsson Linnér, R., et al. (2018). Gene discovery and polygenic prediction from a genome-wide association study of educational attainment in 1.1 million individuals. Nat. Genet. *50*, 1112–1121. https://doi.org/10.1038/s41588-018-0147-3.
45. Okbay, A., Wu, Y., Wang, N., Jayashankar, H., Bennett, M., Nehzati, S.M., Sidorenko, J., Kweon, H., Goldman, G., Gjorgjieva, T., et al. (2022). Polygenic prediction of educational attainment within and between families from genome-wide association analyses in 3 million individuals. Nat. Genet. *54*, 437–449. https://doi.org/10.1038/s41588-022-01016-z.
46. Shadrin, A.A., Kaufmann, T., van der Meer, D., Palmer, C.E., Makowski, C., Loughnan, R., Jernigan, T.L., Seibert, T.M., Hagler, D.J., Smeland, O.B., et al. (2021). Vertex-wise multivariate genome-wide association study identifies 780 unique genetic loci associated with cortical morphology. Neuroimage *244*, 118603. https://doi.org/10.1016/j.neuroimage.2021.118603.
47. Schiller, B.J., Chodankar, R., Watson, L.C., Stallcup, M.R., and Yamamoto, K.R. (2014). Glucocorticoid receptor binds half sites as a monomer and regulates specific target genes. Genome Biol. *15*, 418. https://doi.org/10.1186/s13059-014-0418-y.

48. Smith, D.J., Nicholl, B.I., Cullen, B., Martin, D., Ul-Haq, Z., Evans, J., Gill, J.M.R., Roberts, B., Gallacher, J., Mackay, D., et al. (2013). Prevalence and Characteristics of Probable Major Depression and Bipolar Disorder within UK Biobank: Cross-Sectional Study of 172,751 Participants. PLoS One *8*, e75362. https://doi.org/10.1371/journal.pone.0075362.

49. Bartrés-Faz, D., González-Escamilla, G., Vaqué-Alcázar, L., Abellaneda-Pérez, K., Valls-Pedret, C., Ros, E., and Grothe, M.J. (2019). Characterizing the molecular architecture of cortical regions associated with high educational attainment in older individuals. J. Neurosci. *39*, 4566–4575. https://doi.org/10.1523/JNEUROSCI.2370-18.2019.

50. Ge, T., Chen, C.Y., Doyle, A.E., Vettermann, R., Tuominen, L.J., Holt, D.J., Sabuncu, M.R., and Smoller, J.W. (2019). The Shared Genetic Basis of Educational Attainment and Cerebral Cortical Morphology. Cereb. Cortex *29*, 3471–3481. https://doi.org/10.1093/cercor/bhy216.

51. Kim, J.P., Seo, S.W., Shin, H.Y., Ye, B.S., Yang, J.J., Kim, C., Kang, M., Jeon, S., Kim, H.J., Cho, H., et al. (2015). Effects of education on aging-related cortical thinning among cognitively normal individuals. Neurology *85*, 806–812. https://doi.org/10.1212/WNL.0000000000001884.

52. Vaqué-Alcázar, L., Sala-Llonch, R., Valls-Pedret, C., Vidal-Piñeiro, D., Fernández-Cabello, S., Bargalló, N., Ros, E., and Bartrés-Faz, D. (2017). Differential age-related gray and white matter impact mediates educational influence on elders' cognition. Brain Imaging Behav. *11*, 318–332. https://doi.org/10.1007/s11682-016-9584-8.

53. Kvist, T., Sammallahti, S., Lahti-Pulkkinen, M., Cruceanu, C., Czamara, D., Dieckmann, L., Tontsch, A., Röh, S., Rex-Haffner, M., Wolford, E., et al. (2022). Cohort profile: InTraUterine sampling in early pregnancy (ITU), a prospective pregnancy cohort study in Finland: Study design and baseline characteristics. BMJ Open *12*, e049231. https://doi.org/10.1136/bmjopen-2021-049231.

54. McEwen, B.S., Nasca, C., and Gray, J.D. (2016). Stress Effects on Neuronal Structure: Hippocampus, Amygdala, and Prefrontal Cortex. Neuropsychopharmacology *41*, 3–23. https://doi.org/10.1038/npp.2015.171.

55. Popoli, M., Yan, Z., McEwen, B.S., and Sanacora, G. (2011). The stressed synapse: The impact of stress and glucocorticoids on glutamate transmission. Nat. Rev. Neurosci. *13*, 22–37. https://doi.org/10.1038/nrn3138.

56. Melamed, N., Asztalos, E., Murphy, K., Zaltz, A., Redelmeier, D., Shah, B.R., and Barrett, J. (2019). Neurodevelopmental disorders among term infants exposed to antenatal corticosteroids during pregnancy: a population-based study. BMJ Open *9*, e031197. https://doi.org/10.1136/bmjopen-2019-031197.

57. Räikkönen, K., Gissler, M., and Kajantie, E. (2020). Associations Between Maternal Antenatal Corticosteroid Treatment and Mental and Behavioral Disorders in Children. JAMA *323*, 1924–1933. https://doi.org/10.1001/jama.2020.3937.

58. Tsiarli, M.A., Rudine, A., Kendall, N., Pratt, M.O., Krall, R., Thiels, E., Defranco, D.B., and Monaghan, A.P. (2017). Antenatal dexamethasone exposure differentially affects distinct cortical neural progenitor cells and triggers long-term changes in murine cerebral architecture and behavior. Transl. Psychiatry *7*, e1153. https://doi.org/10.1038/tp.2017.65.

59. Mcewen, B.S. (2005). Glucocorticoids, depression, and mood disorders: structural remodeling in the brain. Metabolism *54* (*Supplement 1*), 20–23. https://doi.org/10.1016/j.metabol.2005.01.008.

60. Schindelin, J., Arganda-Carreras, I., Frise, E., Kaynig, V., Longair, M., Pietzsch, T., Preibisch, S., Rueden, C., Saalfeld, S., Schmid, B., et al. (2012). Fiji: an open-source platform for biological-image analysis. Nat. Methods *9*, 676–682. https://doi.org/10.1038/nmeth.2019.

61. Koyanagi-Aoi, M., Ohnuki, M., Takahashi, K., Okita, K., Noma, H., Sawamura, Y., Teramoto, I., Narita, M., Sato, Y., Ichisaka, T., et al. (2013). Differentiation-defective phenotypes revealed by large-scale analyses of human pluripotent stem cells. Proc. Natl. Acad. Sci. USA *110*, 20569–20574. https://doi.org/10.1073/pnas.1319061110.

62. Okita, K., Matsumura, Y., Sato, Y., Okada, A., Morizane, A., Okamoto, S., Hong, H., Nakagawa, M., Tanabe, K., Tezuka, K.I., et al. (2011). A more efficient method to generate integration-free human iPS cells. Nat. Methods *8*, 409–412. https://doi.org/10.1038/nmeth.1591.

63. Cárdenas, A., Villalba, A., de Juan Romero, C., Picó, E., Kyrousi, C., Tzika, A.C., Tessier-Lavigne, M., Ma, L., Drukker, M., Cappello, S., et al. (2018). Evolution of Cortical Neurogenesis in Amniotes Controlled by Robo Signaling Levels. Cell *174*, 590–606.e21. https://doi.org/10.1016/j.cell.2018.06.007.

64. Saito, T. (2006). In vivo electroporation in the embryonic mouse central nervous system. Nat. Protoc. *1*, 1552–1558. https://doi.org/10.1038/nprot.2006.276.

65. Kyrousi, C., O'Neill, A.C., Brazovskaja, A., He, Z., Kielkowski, P., Coquand, L., Di Giaimo, R., D' Andrea, P., Belka, A., Forero Echeverry, A., et al. (2021). Extracellular LGALS3BP regulates neural progenitor position and relates to human cortical complexity. Nat. Commun. *12*, 6298. https://doi.org/10.1038/s41467-021-26447-w.

66. Jobe, A.H., Kemp, M., Schmidt, A., Takahashi, T., Newnham, J., and Milad, M. (2021). Antenatal corticosteroids: a reappraisal of the drug formulation and dose. Pediatr. Res. *89*, 318–325. https://doi.org/10.1038/s41390-020-01249-w.

67. Kelava, I., Chiaradia, I., Pellegrini, L., Kalinka, A.T., and Lancaster, M.A. (2022). Androgens increase excitatory neurogenic potential in human brain organoids. Nature *602*, 112–116. https://doi.org/10.1038/s41586-021-04330-4.

68. McManus, J.M., and Sharifi, N. (2020). Structure-dependent retention of steroid hormones by common laboratory materials. J. Steroid Biochem. Mol. Biol. *198*, 105572. https://doi.org/10.1016/j.jsbmb.2019.105572.

69. Spoelhof, B., and Ray, S.D. (2014). Fludrocortisone Cortisol/Hydrocortisone. In Encyclopedia of Toxicology, Third Edition, P. Wexler., ed. (Academic Press), pp. 1038–1042. https://doi.org/10.1016/B978-0-12-386454-3.00293-1.

70. Kashiwagi, Y., Kato, N., Sassa, T., Nishitsuka, K., Yamamoto, T., Takamura, H., and Yamashita, H. (2010). Cotylenin a inhibits cell proliferation and induces apoptosis and PAX6 mRNA transcripts in retinoblastoma cell lines. Mol. Vis. *16*, 970–982.

71. Andrews, S., Krueger, F., Segonds-Pichon, A., Biggins, L., and Krueger Christel, M.J. (2019). fastQC. https://www.bioinformatics.babraham.ac.uk/projects/fastqc/.

72. Martin, M. (2011). Cutadapt removes adapter sequences from high-throughput sequencing reads. EMBnet J *17*, 10–12.

73. Krueger, F., and Andrews, S.R. (2011). Bismark: A flexible aligner and methylation caller for Bisulfite-Seq applications. Bioinformatics *27*, 1571–1572. https://doi.org/10.1093/bioinformatics/btr167.

74. Akalin, A., Kormaksson, M., Li, S., Garrett-Bakelman, F.E., Figueroa, M.E., Melnick, A., and Mason, C.E. (2012). MethylKit: a comprehensive R package for the analysis of genome-wide DNA methylation profiles. Genome Biol. *13*, R87. https://doi.org/10.1186/gb-2012-13-10-R87.

75. Benjamini, Y., Krieger, A.M., and Yekutieli, D. (2006). Adaptive linear step-up procedures that control the false discovery rate. Biometrika *93*, 491–507. https://doi.org/10.1093/biomet/93.3.491.

76. Patro, R., Duggal, G., Love, M.I., Irizarry, R.A., and Kingsford, C. (2017). Salmon provides fast and bias-aware quantification of transcript expression. Nat. Methods *14*, 417–419. https://doi.org/10.1038/nmeth.4197.

77. Love, M.I., Huber, W., and Anders, S. (2014). Moderated estimation of fold change and dispersion for RNA-seq data with DESeq2. Genome Biol. *15*, 550. https://doi.org/10.1186/s13059-014-0550-8.

78. Zheng, G.X.Y., Terry, J.M., Belgrader, P., Ryvkin, P., Bent, Z.W., Wilson, R., Ziraldo, S.B., Wheeler, T.D., McDermott, G.P., Zhu, J., et al. (2017). Massively parallel digital transcriptional profiling of single cells. Nat. Commun. *8*, 14049. https://doi.org/10.1038/ncomms14049.

79. Baranwal, A., Bagwe, B.R., and Vanitha, M. (2019). Machine Learning in Python *12*, 128–154. https://doi.org/10.4018/978-1-5225-9902-9.ch008.

80. McInnes, L., Healy, J., and Melville, J. (2018). UMAP: Uniform Manifold Approximation and Projection for Dimension Reduction. Preprint at arXiv. https://doi.org/10.48550/arXiv.1802.03426.

81. Blondel, V.D., Guillaume, J.-L., Lambiotte, R., and Lefebvre, E. (2008). Fast unfolding of communities in large networks. J. Stat. Mech.: Theor. Exp. *2008*, 10008.

82. Wolf, F.A., Hamey, F.K., Plass, M., Solana, J., Dahlin, J.S., Göttgens, B., Rajewsky, N., Simon, L., and Theis, F.J. (2019). PAGA: graph abstraction reconciles clustering with trajectory inference through a topology preserving map of single cells. Genome Biol. *20*, 59. https://doi.org/10.1186/s13059-019-1663-x.

83. Wolf, F.A., Angerer, P., and Theis, F.J. (2018). SCANPY: large-scale single-cell gene expression data analysis. Genome Biol. *19*, 15. https://doi.org/10.1186/s13059-017-1382-0.

84. Finak, G., McDavid, A., Yajima, M., Deng, J., Gersuk, V., Shalek, A.K., Slichter, C.K., Miller, H.W., McElrath, M.J., Prlic, M., et al. (2015). MAST: A flexible statistical framework for assessing transcriptional changes and characterizing heterogeneity in single-cell RNA sequencing data. Genome Biol. *16*, 278. https://doi.org/10.1186/s13059-015-0844-5.

85. Kuleshov, M.V., Jones, M.R., Rouillard, A.D., Fernandez, N.F., Duan, Q., Wang, Z., Koplev, S., Jenkins, S.L., Jagodnik, K.M., Lachmann, A., et al. (2016). Enrichr: a comprehensive gene set enrichment analysis web server 2016 update. Nucleic Acids Res. *44*, W90–W97. https://doi.org/10.1093/nar/gkw377.

86. Chen, E.Y., Tan, C.M., Kou, Y., Duan, Q., Wang, Z., Meirelles, G.V., Clark, N.R., and Ma'ayan, A. (2013). Enrichr: interactive and collaborative HTML5 gene list enrichment analysis tool. BMC Bioinformatics *14*, 128. https://doi.org/10.1186/1471-2105-14-128.

87. Müller-Dott, S., Tsirvouli, E., Vazquez, M., Ramirez Flores, R.O., Badia-i-Mompel, P., Fallegger, R., Türei, D., Lægreid, A., and Saez-Rodriguez, J. (2023). Expanding the coverage of regulons from high-confidence prior knowledge for accurate estimation of transcription factor activities. Nucleic Acids Res. *51*, 10934–10949. https://doi.org/10.1093/nar/gkad841.

88. Badia-i-Mompel, P., Vélez Santiago, J., Braunger, J., Geiss, C., Dimitrov, D., Müller-Dott, S., Taus, P., Dugourd, A., Holland, C.H., Ramirez Flores, R.O., et al. (2022). decoupleR: ensemble of computational methods to infer biological activities from omics data. Bioinform. Adv. *2*, vbac016. https://doi.org/10.1093/bioadv/vbac016.

89. Agrawal Singh, S., Lerdrup, M., Gomes, A.-L.R., van de Werken, H.J.G., Vilstrup Johansen, J., Andersson, R., Sandelin, A., Helin, K., and Hansen, K. (2019). PLZF targets developmental enhancers for activation during osteogenic differentiation of human mesenchymal stem cells. eLife *8*, e40364. https://doi.org/10.7554/eLife.40364.

90. Wu, T., Hu, E., Xu, S., Chen, M., Guo, P., Dai, Z., Feng, T., Zhou, L., Tang, W., Zhan, L., et al. (2021). clusterProfiler 4.0: A universal enrichment tool for interpreting omics data. Innovation (Camb) *2*, 100141. https://doi.org/10.1016/j.xinn.2021.100141.

91. Yu, G., Wang, L.G., Han, Y., and He, Q.Y. (2012). clusterProfiler: an R Package for Comparing Biological Themes Among Gene Clusters. OMICS A J. Integr. Biol. *16*, 284–287. https://doi.org/10.1089/omi.2011.0118.

92. Yu, G. (2023). Enrichplot: Visualization of Functional Enrichment Result. R package version 1.20.0. https://doi.org/10.18129/B9.bioc.enrichplot.

93. Watanabe, K., Taskesen, E., Van Bochoven, A., and Posthuma, D. (2017). Functional mapping and annotation of genetic associations with FUMA. Nat. Commun. *8*, 1826. https://doi.org/10.1038/s41467-017-01261-5.

94. Gene Ontology Consortium (2021). The Gene Ontology resource: Enriching a GOld mine. Nucleic Acids Res. *49*, D325–D334. https://doi.org/10.1093/nar/gkaa1113.

95. Ashburner, M., Ball, C.A., Blake, J.A., Botstein, D., Butler, H., Cherry, J.M., Davis, A.P., Dolinski, K., Dwight, S.S., Eppig, J.T., et al. (2000). Gene ontology: Tool for the unification of biology. Nat. Genet. *25*, 25–29. https://doi.org/10.1038/75556.

96. Buniello, A., Macarthur, J.A.L., Cerezo, M., Harris, L.W., Hayhurst, J., Malangone, C., McMahon, A., Morales, J., Mountjoy, E., Sollis, E., et al. (2019). The NHGRI-EBI GWAS Catalog of published genome-wide association studies, targeted arrays and summary statistics 2019. Nucleic Acids Res. *47*, D1005–D1012. https://doi.org/10.1093/nar/gky1120.

97. Arnold, C.D., Gerlach, D., Stelzer, C., Boryń, Ł.M., Rath, M., and Stark, A. (2013). Genome-Wide Quantitative Enhancer Activity Maps Identified by STARR-seq. Science *339*, 1074–1077.

98. Schöne, S., Bothe, M., Einfeldt, E., Borschiwer, M., Benner, P., Vingron, M., Thomas-Chollier, M., and Meijsing, S.H. (2018). Synthetic STARR-seq reveals how DNA shape and sequence modulate transcriptional output and noise. PLoS Genet. *14*, e1007793. https://doi.org/10.1371/journal.pgen.1007793.

99. Rogatsky, I., Trowbridge, J.M., and Garabedian, M.J. (1997). Glucocorticoid receptor-mediated cell cycle arrest is achieved through distinct cell-specific transcriptional regulatory mechanisms. Mol. Cell. Biol. *17*, 3181–3193. https://doi.org/10.1128/mcb.17.6.3181.

100. The R Core Team (2017). R: A Language and Environment for Statistical Computing. https://www.r-project.org/.

101. Bycroft, C., Freeman, C., Petkova, D., Band, G., Elliott, L.T., Sharp, K., Motyer, A., Vukcevic, D., Delaneau, O., O'Connell, J., et al. (2018). The UK Biobank resource with deep phenotyping and genomic data. Nature *562*, 203–209. https://doi.org/10.1038/s41586-018-0579-z.

102. Elliott, L.T., Sharp, K., Alfaro-Almagro, F., Shi, S., Miller, K.L., Douaud, G., Marchini, J., and Smith, S.M. (2018). Genome-wide association studies of brain imaging phenotypes in UK Biobank. Nature *562*, 210–216. https://doi.org/10.1038/s41586-018-0571-7.

103. van der Loo, M.P.J. (2014). The stringdist package for approximate string matching. The R Journal *6*, 111–122. https://doi.org/10.32614/rj-2014-011.

104. Hemani, G., Zheng, J., Elsworth, B., Wade, K.H., Haberland, V., Baird, D., Laurin, C., Burgess, S., Bowden, J., Langdon, R., et al. (2018). The MR-base platform supports systematic causal inference across the human phenome. eLife *7*, 1–29. https://doi.org/10.7554/eLife.34408.

105. Palmer, T.M., Sterne, J.A.C., Harbord, R.M., Lawlor, D.A., Sheehan, N.A., Meng, S., Granell, R., Smith, G.D., and Didelez, V. (2011). Instrumental variable estimation of causal risk ratios and causal odds ratios in mendelian randomization analyses. Am. J. Epidemiol. *173*, 1392–1403. https://doi.org/10.1093/aje/kwr026.

106. Benjamini, Y., and Hochberg, Y. (1995). Controlling the False Discovery Rate: A Practical and Powerful Approach to Multiple Testing. J. R. Stat. Soc. B Methodol. *57*, 289–300. https://doi.org/10.1111/j.2517-6161.1995.tb02031.x.

107. Faillenot, I., Heckemann, R.A., Frot, M., and Hammers, A. (2017). Macroanatomy and 3D probabilistic atlas of the human insula. NeuroImage *150*, 88–98. https://doi.org/10.1016/j.neuroimage.2017.01.073.

108. Mori, S., Oishi, K., Jiang, H., Jiang, L., Li, X., Akhter, K., Hua, K., Faria, A.V., Mahmood, A., Woods, R., et al. (2008). Stereotaxic white matter atlas based on diffusion tensor imaging in an ICBM template. NeuroImage *40*, 570–582. https://doi.org/10.1016/j.neuroimage.2007.12.035.

109. Hua, K., Zhang, J., Wakana, S., Jiang, H., Li, X., Reich, D.S., Calabresi, P.A., Pekar, J.J., van Zijl, P.C., and Mori, S. (2008). Tract probability maps in stereotaxic spaces: Analyses of white matter anatomy and tract-specific quantification. Neuroimage *39*, 336–347. https://doi.org/10.1016/j.neuroimage.2007.07.053.Tract.

110. Warrington, S., Bryant, K.L., Khrapitchev, A.A., Sallet, J., Charquero-Ballester, M., Douaud, G., Jbabdi, S., Mars, R.B., and Sotiropoulos, S.N. (2020). XTRACT - Standardised protocols for automated tractography in the human and macaque brain. NeuroImage *217*, 116923. https://doi.org/10.1016/j.neuroimage.2020.116923.

111. Masharani, U., Shiboski, S., Eisner, M.D., Katz, P.P., Janson, S.L., Granger, D.A., and Blanc, P.D. (2005). Impact of exogenous glucocorticoid use on salivary cortisol measurements among adults with asthma

and rhinitis. Psychoneuroendocrinology *30*, 744–752. https://doi.org/10.1016/j.psyneuen.2005.03.003.

112. Pruessner, J.C., Kirschbaum, C., Meinlschmid, G., and Hellhammer, D.H. (2003). Two formulas for computation of the area under the curve represent measures of total hormone concentration versus time-dependent change. Psychoneuroendocrinology *28*, 916–931. https://doi.org/10.1016/S0306-4530(02)00108-7.

113. Nancy, B. (2005). Bayley scales of infant and toddler development. https://doi.org/10.1037/t14978-000.

114. Wickham, H. (2016). ggplot2: Elegant Graphics for Data Analysis (Springer-Verlag).

115. Arshadi, C., Günther, U., Eddison, M., Harrington, K.I.S., and Ferreira, T.A. (2021). SNT: a unifying toolbox for quantification of neuronal anatomy. Nat. Methods *18*, 374–377. https://doi.org/10.1038/s41592-021-01105-7.

STAR★METHODS

KEY RESOURCES TABLE

REAGENT or RESOURCE	SOURCE	IDENTIFIER
Antibodies		
GFP, chicken	Aves Laboratory	Cat#GFP-1020; RRID: AB_10000240
PAX6, rabbit	Biozol	Cat#BLD-901301; RRID: AB_3083657
PAX6, mouse IgG1	Abcam	Cat#ab78545; RRID: AB_1566562
SOX2, rabbit	Cell Signaling	Cat#2748; RRID: AB_823640
NEUN, mouse IgG1	Millipore	Cat#MAB377; RRID: AB_2298772
Ki-67, rabbit	Abcam	Cat#ab15580; RRID: AB_443209
BCL11B, rat IgG2a	Abcam	Cat#ab18465; RRID: AB_2064130
TBR1, rabbit	Abcam	Cat#ab31940; RRID: AB_2200219
SATB2, mouse IgG1	Abcam	Cat#ab51502; RRID: AB_882455
EOMES, rabbit	Abcam	Cat#ab23345; RRID: AB_778267
EOMES, sheep	R&D Systems	Cat#AF6166; RRID: AB_10569705
MAP2, chicken	Abcam	Cat#ab5392; RRID: AB_2138153
ZBTB16, mouse IgG2a	Active Motif	Cat#39988; RRID: AB_2793419
ZBTB16, mouse IgG1	Santa Cruz	Cat#sc-28319; RRID: AB_2218941
ACTIN, rabbit	Cell Signaling	Cat#4967; RRID: AB_330288
BrdU, rat	Abcam	Cat#ab6326; RRID: AB_305426
Chicken-Alexa Fluor 488, donkey	Dianova	Cat#703-545-155; RRID: AB_2340375
Rabbit-Alexa Fluor 647, donkey	Dianova	Cat#711-606-152; RRID: AB_2340625
Mouse-Alexa Fluor 594, donkey	Dianova	Cat#715-585-150; RRID: AB_2340854
Rat-Alexa Fluor 647, goat	Abcam	Cat#ab150167; RRID: AB_2864291
Sheep-Alexa Fluor 594, donkey	Dianova	Cat#713-585-147; RRID: AB_2340748
Rabbit-HRP linked, goat	Cell Signaling	Cat#7074; RRID: AB_2099233
Mouse-HRP linked, horse	Cell Signaling	Cat#7076; RRID: AB_330924
Bacterial and virus strains		
DH5-Alpha competent cells	Thermo Fisher Scientific	18265017
StellarTM competent cells- HST08	Takara	639298
Chemicals, peptides, and recombinant proteins		
S.P. HiFi Cas9 V3 nuclease	IDT DNA Technologies	Cat#1081060
Deposited data		
Bulk RNA-seq of No.1 hCOs with dexamethasone 100nM for 7 days	BioProject	PRJNA865917
MRa-PheWAS	OSFHome	https://osf.io/4ud6q/
Single cell sequencing of day 30 No.1 hCOs with dexamethasone 100nM for 12 hours	Cruceanu et al.[16]	GEO: GSE189534
Single cell sequencing of day 70 HPS0076 hCOs with dexamethasone 100nM for 10 days	Zenodo	https://doi.org/10.5281/zenodo.10391946
Targeted Bisulfite Sequencing of the *ZBTB16* locus in No.1 hCOs treated with dexamethasone 100nM for 7 days	BioProject	PRJNA1050905
Experimental models: Cell lines		
HPS0076 iPSCs	RIKEN BRC cell bank	HPS0076-409b2
No.1 iPSCs	GlobalStem	GSC-3404

(*Continued on next page*)

Continued

REAGENT or RESOURCE	SOURCE	IDENTIFIER
HELA	N/A	RRID: CVCL_0030
Experimental models: Organisms/strains		
C57BL/6J	Jackson Laboratory	RRID: IMSR_JAX:000664
Oligonucleotides		
hZBTB16- qPCR hMAP2 – qPCR hPOLR2A-qPCR hYWHAZ - qPCR	IDT	Hs.PT.58.605743 Hs.PT.58.20103440 Hs.PT.39a.19639531 Hs.PT.39a.22214858
DNA GFP- STARR qPCR	IDT	fwd-5'CCAGCTGTTGGGGTGTCCA rev-5'GACAGAGAACTTGTGGCCGT
DNA RPL19- STARR qPCR	IDT	fwd-5'TCGCCTCTAGTGTCCTCCG rev-5'GCGGGCCAAGGTGTTTTTC
mRNA GFP- STARR qPCR mRNA RPL19-STARR qPCR STARR qPCR vector- sanger seuqncing	IDT	5'CAAACTCATCAATGTATCTTATCATG5'GAGGCCAGTATGTACAGACAAAGTGG5'GCGATGGCCCTGTCCTTTTA
ZBTB16 Exon 2 - CRISPR	IDT	fwd-5'GGAAGGGGCTAAAGTCTTGCTrev-5'TAGGCCCCCTCACTACACTT
rs648044- CRISPR	IDT	fwd-5'GACCTGGACTTGTTGGGGAGrev-5'TTCACCCTCCATCAGGGCTA
crRNA upstream ZBTB16 exon 2crRNA downstream of rs648044crRNA upstream of rs648044crRNA downstream ZBTB16 exon 2	IDT	GTTGCCAAGCCCTTAGCAAG CAAGTCC TACATCAGGTGCG ATGGGTCTACTCTAC AGACC TCTCAGAAGGGCCTCCTACA
HAM-TBS and Pyrosequencing	See Table S1	N/A
Recombinant DNA		
pCAG-DsRed2	Addgene	Cat#15777
Snap25-LSL-2A-GFP	Addgene	Cat#61575
pCAG-F2A-GFP	produced in this study	N/A
pCAG-ZBTB16-F2A-GFP	produced in this study	N/A
Software and algorithms		
GraphPad Prism 9	Dotmatics	Academic module
Fiji is just ImageJ 2.1	Nature Methods	Schindelin et al.[60]
SnapGene	Dotmatics	Academic module

RESOURCE AVAILABILITY

Lead contact

Further information and requests for resources and reagents should be directed to and will be fulfilled by the lead contact, Prof. Dr. Elisabeth Binder (binder@psych.mpg.de).

Materials availability

Plasmids and iPSC lines generated in this study are available upon request. Human iPSC lines used in this study are subject to MTA approvals.

Data and code availability

- Bulk and single-cell RNA-seq data have been deposited at GEO, Bioproject or Zenodo and are publicly available as of the date of publication. Accession numbers are listed in the key resources table. Microscopy data reported in this paper will be shared by the lead contact upon request.
- All original code has been deposited at Zenodo and is publicly available as of the date of publication. DOIs are listed in the key resources table.
- Any additional information required to reanalyse the data reported in this paper is available from the lead contact upon request.

EXPERIMENTAL MODEL AND STUDY PARTICIPANT DETAILS

Cell lines

HPS0076 human induced pluripotent stem cells (hiPSCs) were obtained from the RIKEN BRC cell bank and reprogrammed from skin fibroblasts of a female donor (HPS0076-409b2).[61,62] No.1 hiPSCs were reprogrammed from NuFF3-RQ newborn foreskin feeder fibroblasts of a male donor (GSC-3404, GlobalStem).[63] MTA approvals were obtained for the use of both hiPSC lines. hiPSCs were cultured in Matrigel-coated (1:100 diluted in DMEM-F12 (Gibco, 31330-038), Corning Incorporated, 354277) Costar 6-well cell culture plates (Corning Incorporated, 3516) in mTESR1 Basal Medium (STEMCELL Technologies, 85851) supplemented with 1x mTESR1 Supplement (STEMCELL Technologies, 85852) at 37°C with 5% CO_2. Passaging was performed with Gentle Cell Dissociation Reagent (STEMCELL Technologies, 07174). RevitaCell Supplement (1:100 diluted, Gibco, A2644501) was added the day of the dissociation for 24h to increase cell survival.

Cerebral organoids

Human cerebral organoids (hCOs) were created as previously described by Lancaster et al.[15] with some modifications. Briefly, hiPSCs were dissociated in StemPro Accutase Cell Dissociation Reagent (Life Technologies, A1110501). Nine thousand single cells were plated into Ultra-low attachment 96-well plate round bottom wells (Corning Incorporated, 7007) in human embryonic stem cell medium (hESC, DMEM/F12-GlutaMAX (Gibco, 31331-028) with 20% Knockout Serum Replacement (Gibco, 10828-028), 3% FBS (Fetal Bovine Serum, Gibco, 16141-061), 1% non-essential amino acids (Gibco, 11140-035), 0.1 mM 2-mercaptoethanol (Gibco, 31350-010)) supplemented with 4 ng/ml human recombinant FGF (Fibroblast Growth Factor, Peprotech, 100-18B) and 50 μM Rock inhibitor Y27632 (Millipore, SCM075) for 4 days and in hESC medium without bFGF and Rock inhibitor for an additional 2 days to form embryoid bodies (EBs). On day 6, the medium was changed to neural induction medium (NIM, DMEM/F12 GlutaMAX supplemented with 1:100 N2 supplement (Gibco, 15502-048), 1% Non-essential amino acids and 1 μg/ml Heparin (Sigma, H3149)) and cultured for an additional 6 days. On day 12, the EBs were embedded in Matrigel (Corning Incorporated, 354234) drops and transferred to 10-cm cell culture plates (TPP, 93100) in neural differentiation medium without vitamin-A (NDM-A, DMEM/F12GlutaMAX and Neurobasal (Gibco, 21103-049) in ratio 1:1 supplemented with 1:100 N2 supplement, 1:100 B27 without Vitamin A (Gibco, 12587-010), 0.5% non-essential amino acids, insulin 2.5 μg/ml (Gibco, 19278), 1:100 Antibiotic-Antimycotic (Gibco, 15240-062) and 50 μM 2-mercaptoethanol) for 4 days. On day 16, hCOs were transferred onto an orbital shaker in NDM+A medium (same composition as NDM-A with the addition of B27 with Vitamin A (Gibco, 17504-044) in the place of B27 without Vitamin A) and were grown in these conditions at 37°C with 5% CO_2. NDM+A medium was changed twice per week.

Mice

All experiments and protocols were performed in accordance with the European Communities' Council Directive 2010/63/EU and were approved by the committee for the Care and Use of Laboratory Animals of the Government of Upper Bavaria. All mice (*Mus musculus*; C57BL/6J, Jackson laboratory) were obtained from the in-house breeding facility of the Max Planck Institute of Psychiatry and kept in group housed conditions in individually ventilated cages (IVC; 30 cm x 16 cm x 16 cm; 501 cm^2) serviced by a central airflow system (Tecniplast, IVC Green Line – GM500). Animals had ad libitum access to water (tap water) and standard chow and were maintained under constant environmental conditions (12:12 h light/dark cycle, 23 ± 2°C and humidity of 55%). Female mice were time-mated and used at embryonic day 13.5 or 14.5 for *in utero* electroporations. Embryos of both sexes were electroporated as at these developmental stages sex differentiation is not possible.

METHOD DETAILS

In utero electroporations of mice

Time-pregnant female mice at stage E13.5 or E14.5 were anesthetized by intraperitoneal injection of saline solution containing fentanyl (0.05 mg per kg body weight), midazolam (5 mg per kg body weight), and medetomidine (0.5 mg per kg body weight) and embryos were electroporated as described by Saito et al.[64] In brief, plasmids were mixed with Fast Green (2.5 mg/μL; Sigma F7252) and approx. 1 μl was injected at a final concentration of 1μg/μL using glass micropipettes (5-000-1001-X10, Drummond Scientific). The DNA was electroporated into the cells by delivering 5 pulses applied at 40V for 50 ms in 1 s intervals. Anesthesia was terminated by injection of buprenorphine (0.1 mg per kg body weight), atipamezole (2.5 mg per kg body weight), and flumazenil (0.5 mg per kg body weight). The pups remained *in utero* for 3 or 6 more days, after which euthanizing occurred and the pups' brains were isolated. Brains were fixed in 4% PFA (paraformaldehyde) for 16 h, cryo-preserved with 30% sucrose for at least 16 h and stored at −20°C in OCT (optimal cutting temperature, Thermo Fischer Scientific, 23-730-571). For immunofluorescence, 12 μm cryosections were prepared on SuperFrost™ slides. For the cell cycle re-entry experiment, embryos were electroporated at E13.5 and the mother received an intraperitoneal injection of 100 mg/kg of body weight of BrdU diluted in saline at E15.5, 24 hours before sacrifice at E16.5.

Electroporations of human cerebral organoids

HPS0076-hCOs were electroporated as described in Kyrousi et al.[65] In brief, hCOs were kept in antibiotic-free NDM+A medium for three hours prior to electroporation. Electroporation was performed in hCOs at day 43 after the initial plating of the cells, and hCOs

were fixed at 7 dpe. During electroporation, hCOs were placed in an electroporation chamber (Harvard Apparatus, Holliston, MA, USA) under a stereoscope. Using a glass micropipette (5-000-1001-X10, Drummond Scientific) 0.5 μL of plasmid DNA was injected together with Fast Green into different ventricles at a final concentration of 1 μg/μL. hCOs were subsequently electroporated with 5 pulses applied at 80 V for 50 ms each, at 500 ms intervals (ECM830, Harvard Apparatus). Following electroporation, hCOs were kept for an additional 24 h in antibiotics-free NDM+A media and then changed into the normal NDM+A media until fixation at 7 dpe. hCOs were fixed using 4% PFA for 1 h at 4°C, cryo- preserved with 30% sucrose for 16 h and stored at −20°C in OCT. For immunofluorescence, 16 μm cryosections were prepared on SuperFrost™ slides.

Glucocorticoid treatment in cerebral organoids and mice

hCOs

Day 43 hCOs of both lines were treated for 7 days with 100 nM of dexamethasone (dex). To achieve the concentration used, dex was diluted in DMSO (dimethyl sulfoxide) in a concentration of 100 μM and subsequently diluted in NDM+A culture medium to a final concentration of 100 nM. The DMSO control (vehicle- veh) underwent the same dilutions as described for dex. The medium was changed every two days. At the end of the treatment, hCOs were fixed using 4% PFA for 1 h at 4°C, cryo-preserved with 30% sucrose for 16 h and stored at −20°C in OCT. For immunofluorescence, 16 μm cryosections were prepared on SuperFrost™ slides.

Concentration and timing rationale

The concentration of 100 nM was chosen to mimic the antenatal corticosteroid therapy scheme used during pregnancy. The guidelines for sGC use are four doses of 6 mg dex every 12 h given intramuscularly[8,66] when used in at risk for preterm birth pregnancies. A single dose of 6 mg reaches a C_{max} of 65-95 ng/μl at T_{max} 3 h[66] which equals to a concentration of ∼162 nM-245 nM, whereas 1.5 mg would equal to ∼40.4 nM-61.25 nM. The maternal to fetal steroid hormones ratio has been reported anywhere from 0.4 and higher, days after the treatment.[66] So, from a single 6 mg dose we would expect at the very least ∼64.8 nM-98 nM reaching the fetus 3 h post treatment. Similarly, from 1.5 mg given each day we would expect at least ∼16.16 nM-39.2 nM reaching the fetus 3 h post treatment. A previously published study that used 100 nM of androgens, which are also steroid hormones, in hCOs measured an actual concentration of 16 nM.[67] They attributed this phenomenon to the fact that steroid hormones have high affinity to plastic due to their lipophilic nature.[68] Since our primary aim was to study the role of sGC therapy schema, the use 100 nM of dex should parallel the amounts reaching the embryo by the clinically used concentrations. As mentioned, the schema of antenatal corticosteroids treatment is four doses during a 2 days' time. Dexamethasone is a long-acting corticosteroid with a biological half-life of 36 to 54/72 h.[69] Considering the active administration time and the biological half-life of the steroid, we would expect dex effects on the fetus for 5-7 days, with peak exposure for 2-3 days and then a decrease. Thus, we chose to administer dex for 7 days.

Immunofluorescence

Sections were post-fixed in 4% PFA for 10 min at RT and permeabilized with 0.3% Triton in PBS for 5 min. Sections were subsequently blocked with 0.1% TWEEN, 10% Fetal Bovine Serum and 3% BSA. Primary and secondary antibodies (see key resources table) were diluted in blocking solution and nuclei were visualized using 0.5 μg/mL 4,6-diamidino-2-phenylindole (DAPI, Sigma Aldrich). Cover slips were mounted with Aqua Poly/Mount (Polysciences, 18606-20). For PAX6, EOMES, BCL11B, ZBTB16, SOX2, Ki-67, TBR1 and SATB2 antigen retrieval was performed before post-fixing with PFA. Briefly, sections were incubated with citric buffer (0.01 M, pH 6.0) for 1 min at 720 Watt and 10 min at 120 Watt, left to cool down at RT for 20 min and washed three times with PBS for 5 min.

Protein isolation and western blot

Proteins were isolated on ice in RIPA buffer (Sigma-Aldrich, R0278) supplemented with protease (Sigma Aldrich, P8340) and phosphatase inhibitors (Sigma Aldrich, 4906845001). For each experiment three biological replicates were included each bearing the homogenate of three individual hCOs. 30 μg of protein extracts were separated by SDS-PAGE with an 8% gel. Proteins were transferred to a PVDF membrane (Millipore, IPVH00010). For detection, membranes were incubated with primary antibodies (key resources table) for 16 h at 4°C and with horse- radish peroxidase-labeled secondary antibodies (key resources table) at RT for 1 h. Subsequently, they were treated with Immobilon Western HRP Substrate Luminol Reagent and Solution (Millipore, WBKLS0500) to visualize the bands. The quantification was performed in the Bio-Rad Image Lab Software (Version 6.1). Relative protein expression levels were quantified and normalized with ACTIN as endogenous control.

RNA isolation and quantitative PCR

Total RNA was extracted from hCOs using the RNeasy Mini extraction kit (Qiagen, 74104) according to the manufacturer's instructions. For each experiment three biological replicates were included each bearing the homogenate of three individual hCOs. Complementary DNA (cDNA) synthesis was performed using the Maxima H Minus Reverse Transcriptase (Thermo Fisher, EP0751) with oligo(dT)16 primers (Invitrogen, N8080128) and random hexamers (IDT DNA Technologies, 51-01-18-25) in a 1:1 ratio. Quantitative PCR (RT-qPCR) reactions were run in quadruplicate using PrimeTime qPCR Primer Assays (IDT DNA Technologies, key resources table) and PrimeTime® Gene Expression Master Mix (IDT DNA Technologies, 1055770) on a LightCycler 480 Instrument II (Roche). Relative gene expression levels were quantified using the relative quantification method and normalized with POLR2A and YWHAZ as endogenous control genes. Data shown are additionally normalized over the vehicle samples so that vehicle samples have values of approximately one.

Plasmids preparation

Multiple PCR inserts were simultaneously cloned by In-Fusion HD Cloning Plus into the linearized vector pCAG-DsRed2 (Addgene, #15777) to create the pCAG-ZBTB16-F2A-GFP plasmid. More specifically, the human ZBTB16 ORF (NM_006006.5, 2034 bp) sequence was amplified from a plasmid delivered from GenScript and the F2A-GFP from the Snap25-LSL-2A-GFP vector (Addgene, #61575). PCR primers were designed for the sequence of interest with extensions that are complementary to the ends of the linearized vector or the corresponding fragment (key resources table). PCR was performed using the CloneAmp HiFi PCR Premix (Takara Bio, 639298) following manufacturer's instructions

After cloning the fragments for 3 h at 37°C, the new construct was transformed into StellarTM competent cells and grown for 16 h on agar plates containing 100 μg/ml ampicillin. Single colonies were picked, plasmidic DNA was isolated with Qiagen plasmid kits (12123, 12143) and the genotype was checked with Sanger sequencing. The pCAG-F2A-GFP plasmid was created by cutting the ZBTB16 fragment out of the pCAG-ZBTB16-F2A-GFP plasmid using the BamHI and BglI restriction enzymes.

Luciferase reporter assays

Luciferase assays were designed to assess the activity of the three human *PAX6* promoters,[70] P0, P1 and Pa under ZBTB16 overexpression. The promoter sequences were cloned into the firefly luciferase (Luc2) reporter expression pRP vector by VectorBuilder. The human ZBTB16 expression plasmid was generated by VectorBuilder using the pRP backbone. 500 ng of total plasmid DNA (75% of human ZBTB16 expression plasmid, 15% of reporter plasmid and 10% of the pCAG-F2A-GFP, as internal control of transfection efficiency) were transfected into 72,000 HeLa cells in a well of a 24 well plate using Lipofectamine 2000 (ThermoFisher Scientific) following manufacturer's instructions. All transfections were carried out in triplicates. HeLa cells were cultured in DMEM-F12 medium (Gibco, 11320033) supplemented with 10% FBS (Gibco, 16141-061) and 1x Antibiotic-Antimycotic (Gibco, 15240-062). The medium was refreshed the next day and 48 h later transfected cells were PBS washed and incubated for 15 min at RT in 1x passive lysis buffer (Biotium, 99821). Plates were kept at least 1 h at -80°C. Next, the lysate was scraped and centrifuged at full speed for 30 s at 4°C. 20 μl of the supernatant was subjected to the luciferase assay with the addition of 50 μl D-luciferine (Beetle Juice luciferase assay, PJK, 102511-1) by using a Tristar multimode reader (Berthold). The luminescence measurement was done for 5 s using 2 s delay. In addition, 50 μl of the lysate were assessed for GFP fluorescence. The luciferase reading was normalized over the GFP results for each well. Data is shown as fold changes over the control plasmid.

CRISPR-Cas9 editions of hiPSCs

CRISPR-Cas9 editing was used to create genomic deletions of the *ZBTB16* exon 2 and of 744 bp of the regulatory element centered on rs648044 an intronic *ZBTB16* variant. Genome editing was done by electroporation of gRNA pairs (crRNA/tracrRNA duplexes, alt-CRISPR IDT) and recombinant S.P. HiFi Cas9 V3 nuclease (IDT DNA Technologies, 1081060). crRNAs were designed using the Benchling webtool and analysed for self- or heterodimers using the IDT OligoAnalyser™ tool (key resources table). To delete the region of interest, 300,000 No.1 iPSCs were transfected with 35 pmol of each gRNA (crRNA/tracrRNA duplex 1:1 in 1x Arci annealing buffer (STEMCELL Technologies, 76020), IDT DNA Technologies), 40pmol of Cas9 and 100pmol of electroporation enhancer (IDT DNA Technologies, 1075915) in 26.57 μl of the P3 primary cell 4D_X Kit S (Lonza, V4XP-3032) using the 4D-Nucleofector X Unit (Lonza, AAF-1003X) with the CA-137 program. Edited cells were plated into one well of 24-well plate coated with Matrigel 1:100 and cultured in supplemented mTESR1 Basal Medium and, for the day of the edition, with RevitaCell (1:100) at 37°C with 5% CO_2. For control editions, cells were electroporated with Cas9 without the addition of gRNAs. The next day the medium was changed to supplemented mTESR1 and cells were propagated approximately for 2-3 days till they reached 80-90% confluence. Next, cells were passaged into a well of a 6-well plate coated with Matrigel using Gentle Cell Dissociation Reagent and propagated until confluence. Subsequently, 89.5% of the cells were expanded, 10% of them were taken for bulk genotyping analysis and 0.5% were plated in a well of a 6-well plate coated with Matrigel to generate single-cell-derived clonal cell lines. Bulk and single cell DNA extraction was done using 30 μl of QuickExtract DNA Extraction Solution (Lucigen, QE09050). Briefly, cells were dissociated, pelleted, resuspended in the extraction solution and incubated at 65°C for 10 min and 98°C for 5 min. PCR was performed using the primers in key resources table, the Q5 high fidelity master mix (New England Biolabs, M0494S) and 40ng of cell extract in a total volume of 10 μl. The thermal cycling profile of the PCR was: 98°C 30 s; 35 × (98° 10 s, 65°C 15 s, 72°C 60 s); 72°C 2 min. Automated electrophoresis technique (DNA screen tape analysis, Agilent) and Sanger sequencing (Eurofins, primers in key resources table) were used to confirm the presence of CRISPR-Cas9-mediated knockout mutants in the bulk population and the single clones. For the *ZBTB16* exon 2 edition we selected a heterozygous KO cell line (termed ZBTB16$^{+/-}$ and ZBTB16$^{+/+}$ for the control edition) showing by western-blot analysis a ~46% reduction in protein expression (key resources table). The rs648044 is a heterozygous SNP in the iPSC cell line used (rs648044$^{G/A}$). From the edited single clones, we selected a heterozygous KO cell line of the enhancer element harboring the A genotype (termed rs648044$^{G/-}$ and rs648044$^{G/A}$ for the control edition). The effect of the KO on *ZBTB16* expression was assessed by RT- qPCR in veh and dex conditions and using *POLR2A* and *YWHAZ* for normalization (key resources table).

Flow cytometry

No.1- ZBTB16$^{+/+}$ and ZBTB16$^{+/-}$ hCOs were collected for Flow Cytometry analysis (FCa) at day 50 after 7 days of treatment with veh or 100nM dex and/or 1μM of the GR antagonist RU-486 (Selleck, S2606). Three to four samples per batch were analysed and each sample contained two individual hCOs. hCOs were enzymatically dissociated with accutase supplemented with DNase I

(ThermoFisher Scientific, EN0521) at 37°C for maximum 40 min. During incubation, every 10 min the hCOs were additionally manually dissociated with a P1000 pipette. Once dissociated, the hCOs were centrifuged for 5 min at 300g and the pellet was resuspended in PBS to wash. Next, cells were centrifuged and the cell pellets were fixed with 70% EtOH at -20°C for 1 h. Subsequently, after the addition of 5 ml washing buffer (PBS + 1% FBS) fixed cells were centrifuged for 30 min, at 4°C and 500g. The cell pellet was resuspended in 200 μl staining solution (wash buffer supplemented with anti-PAX6 and anti-EOMES, key resources table) and incubated for 30 min on ice. After the primary antibody incubation, 1 ml of washing buffer was added and the stained cells were centrifuged for 30 min, at 4°C, at 500g. The cell pellet was resuspended in 200 μl secondary antibody staining solution (wash buffer supplemented with anti-rabbit 488, anti-sheep 594 and DAPI, key resources table) and incubated for 30 min on ice. The stained cells were filtered through an 100 μm cell strainer and diluted in additional 200 μl wash buffer. FCa was performed at a FACS Melody (BD) in BD FACS Flow TM medium, with a nozzle diameter of 100 μm. For each run, 20,000 cells were analysed. For the 488 fluorophore we used the 488 nm laser coupled with the 530/30 filter and for the 594 fluorophore we used the 561 nm laser coupled with the 613/18 filter. *Gating strategy*: SSC-A/FSC-A gates were used to exclude cell debris and FSC-H/ FSC-W to collect single cells. Gating for fluorophores was done using samples stained with secondary antibody only. The flow rate was set below 30 events/s. Further analysis was done using the software of the FACS Melody (BD) and the online free software Floreada.io.

Targeted bisulfite sequencing

Targeted bisulfite sequencing was performed following the original protocol.[41] DNA was isolated from day 30 hCOs that were treated with 100 nM dex or veh for 7 days with the NucleoSpin Genomic DNA kit (Macherey-Nagel). Bisulfite treatments were performed in triplicate for 200 ng of DNA from each sample with the EZ DNA Methylation Kit (Zymo Research, D5001) and then pooled to run one PCR amplification per amplicon to reduce cost and maximize the number of samples per sequencing run. Twenty nanograms of bisulfite-converted DNA and 49 amplification cycles were then used for each PCR amplification (Table S1) with the Takara EpiTaq HS Polymerase (Clontech, R110A). PCR amplicons were then quantified with an automated electrophoresis technique (2200 DNA screen tape analysis, Agilent) and pooled in equimolar quantities for each sample. AMPure XP beads (Beckman Coulter, A63880) were used for a double size selection (200–500 bp) to remove primer dimers and high molecular DNA fragments. Libraries were generated using the TruSeq DNA PCR-Free HT Library Prep Kit (Illumina, 20015963) according to the manufacturer's instructions. Each library was quantified with the Qubit® 1.0 (ThermoFisher Scientific), normalized to 4 nM and pooled. Library concentration and fragment sizes were checked with the Agilent's 2100 Bioanalyser (Agilent Technologies) and quantitative PCR using the Kapa HIFI Library quantification kit (Kapa Biosystems, KK4824). Paired-end sequencing was performed on an Illumina MiSeq Instrument (Illumina) with their MiSeq Reagent Kit v3 (MS-102-3001, 2Å~300 cycles) with the addition of 15% of PhiX Control v3 library (Illumina, FC-110-3001) generating 300 bp long paired-end reads. Reads were processed as described by Roeh et al.[41] In brief, read quality was verified using FastQC,[71] and cutadapt v1.11[72] was applied to trim reads. Subsequently, reads were aligned to a restricted reference consisting of the amplicon sites using Bismark v0.18.2.[73] Paired-end reads were stitched together using an in-house perl script. Using the R package methylKit v.1.6.3[74] increasing Phred score quality cutoff to 30, methylation levels were extracted. Further filtering was conducted in R. We excluded artifacts on a per sample basis, including low-coverage amplicons (sequencing coverage < 1000, 0 samples excluded) and samples with bisulfite conversion efficiency lower 95% (0 samples excluded). To test for significance, individual CpGs of the same enhancer element were tested with two-way ANOVA and corrected for multiple comparisons with the two-stage step-up method of Benjamini, Krieger and Yekutieli.[75]

Methylation analysis by bisulfite pyrosequencing

DNA was isolated from day 30 hCOs that were treated with 100 nM dex or veh for 7 days with the NucleoSpin Genomic DNA kit (Macherey-Nagel). Bisulfite treatments were performed in triplicate for 300 ng of DNA from each sample with the EZ DNA Methylation Kit (Zymo Research, D5001) and then pooled to run one PCR amplification per amplicon in order to reduce cost and maximize the number of samples per sequencing run. Twenty nanograms of bisulfite-converted DNA and 45 amplification cycles were then used for each PCR amplification (Table S1) with the PyroMark PCR Kit (Qiagen, 978703). Pyrosequencing primers were designed with the MethMarker software and carried out on a PyroMark Q48 Autoprep using PyroMark Q48 Magnetic Beads (cat. no. 974203), PyroMark Q48 Discs (cat. no. 974901) and PyroMark Q48 Absorber Strips (cat.no. 974912), according to the manufacturer's recommendations. To test for significance, individual CpGs were tested with two-way ANOVA and corrected for multiple comparisons with the two-stage step-up method of Benjamini, Krieger and Yekutieli.[75]

Bulk RNA sequencing

RNA was isolated from day 45 No.1- hCOs in triplicates with 2–3 organoids pooled per replicate, either treated with 100 nM dex for 7 days or veh (DMSO). Sequencing libraries were prepared using the QuantSeq 3′ mRNA Fwd kit (Lexogen) following manufacturer's instructions. Sequencing was performed on an Illumina HiSeq4000 sequencer generating 150 bp long single-end reads. Read quality was verified using FastQC version 11.4.[71] For adapter trimming and quality filtering the software cutadapt version 1.9.1[72] was used. For read alignment and gene quantification salmon version 0.43.1[76] was applied setting the parameters noLengthCorrection and perTranscriptPrior to account for the tag sequencing approach. Differential gene expression was assessed using the R package DESeq2.[77] Data are openly available as BioProject with accession number PRJNA865917.

HPS0076 chronic single-cell dataset

Single-cell RNA-sequencing data of 70-day-old hCOs (HPS0076 derived) treated with 100 nM of dexamethasone for 10 days prior to collection were obtained from https://zenodo.org/records/10391946. We sub-setted the dataset to cells from 70-day-old organoids and recomputed 4000 highly variable genes (HVGs) (using log-normalized counts and the "cell_ranger" flavor[78]), principal components,[79] a nearest neighbor graph,[80] louvain clustering (https://github.com/vtraag/louvain-igraph),[81] and partition-based graph abstraction (PAGA)[82] using default parameters in scanpy[83] v1.9.3. The layout obtained from plotting the PAGA results with a threshold of 0.01 was used as initialization to compute Uniform Manifold Approximation and Projection (UMAP)[80] with default parameters.

We used the MAST R package[84] v1.20.0 (R v4.1.2) to compute differential expression between different groups of cells as specified below. Unless stated otherwise, we only used cells from samples with more than 10 cells in the dataset. We furthermore removed any genes which were expressed in less than 5% of the cells and controlled for the number of expressed genes in the expression model. We used the likelihood ratio test to compute the statistical significance of differential expression and corrected for multiple testing using false discovery rate (FDR) correction.

Differential expression was computed for the following groups: between treatment and control for each of the eight cell-types in the dataset; between *ZBTB16* positive and negative cells in the combined population of vehicle-treated Radial Glia and Intermediate Progenitor cells; between treatment and control in cells positive for *PAX6* and *EOMES* (due to low cell numbers in this case without the filtering of samples containing more than 10 cells); between treatment and control in progenitors (combining the RG, Cycling and IP clusters) and all non-progenitors (all remaining clusters).

Enrichment of *ZBTB16* target genes in the progenitors and non-progenitors significant DE genes (treatment vs. control; FDR corrected p value > 0.05) was computed using the Python implementation of Enrichr[85,86] via the GSEApy[83] package v1.0.5 with default parameters. *ZBTB16* target genes were obtained from the CollectTRI[87] database, via the Python implementation of decoupler[88] v1.4.0. This analysis was repeated with manually adding *PAX6* (found as a target in Singh et al.[89]) as an additional target gene of *ZBTB16* in an otherwise identical setting.

For Gene Set Enrichment Analysis, we used the R package Cluster Profiler (release 3.17)[90,91] and plotted the results using EnrichPlot.[92]

For overrepresentation analysis for the DE genes in progenitor and non-progenitor clusters we used FUMA GENE2FUNC[93] analysis based on Gene Ontology (GO, [94,95], analysis references the NHGRI-EBI GWAS Catalog[96] (https://www.ebi.ac.uk/gwas/) most recently updated on 27 September 2023). Default parameters were used in FUMA, with all genes expressed in either the progenitor or the non-progenitor DE analysis as the background list. We used an FDR cutoff of 5% for statistical significance.

No.1 single-cell dataset

Uniform Manifold Approximation and Projection plots (UMAP)[80] were used to visualize the expression of five genes (*ZBTB16, PAX6, TSC22D3, KLF9, HEYL*) in a previously published single-cell RNA seq dataset (Cruceanu et al.[16]). Specifically, gene expression was plotted in the day 30 subsets from cell-line 1 of the aforementioned dataset using the SCANPY[83] python package. The software environment and data processing used to produce these Figure s was identical to the environment and processing steps used to produce expression-UMAPs in Cruceanu et al.[16] Using the same data subset, the number of cells positive (>0 raw counts) and negative (0 raw counts) for the five genes were computed across the cell-type clusters defined in the associated publication. The percentages of the positive, for each gene, cells in each cluster depicted in Figure S3B were calculated as a fraction of the total cells positive for each gene in all clusters using the Wilson/Brown method with 95% confidence intervals.

STARR (Self-Transcribing Active Regulatory Region sequencing)-qPCR

rs648044 cloning into STARR reporter plasmid

For the STARR-qPCR assay, candidate sequences were cloned in the 3′-UTR of the sgGFP reporter gene driven by the SCP1 minimal promoter.[97] Once transfected into GR expressing cells, active regulatory elements would modulate GFP expression under dex treatment.[98] 201 bp long DNA inserts (gblock, IDT) containing 200 bp putative regulatory element centered on the rs648044 (reference and alternative allele) and flanked by 15bp sequence homologous to the STARR reporter construct (key resources table) were inserted by in-Fusion HD Cloning Plus into the human STARR-seq vector digested with SalI and AgeI following the manufacturer's instructions (Takara Bio, 102518). The inserts had additionally 2 bp to reconstitute the AgeI and SalI restriction sites lost during cloning. Subsequently, the constructs were transformed into Stellar™ competent cells (Takara Bio, 636763) and grown for 16 h on agar plates containing 100 μg/ml ampicillin. Single colonies were picked, plasmidic DNA was isolated with Qiagen plasmid kits (12123, 12143) and the genotype was checked with Sanger sequencing (key resources table).

U2OS-GR18 cells transfection

U2OS cells stably transfected with rat GRα (GR18 cells)[99] were cultured in Dulbecco's Modified Eagle Medium- high glucose supplemented (Gibco, 11965084) with 10% FBS (Gibco, 16141-061) and 1x Antibiotic-Antimycotic (Gibco, 15240-062). Two million cells were transfected with 2 μg of plasmid in triplicates using the Amaxa Nucleofector II Kit V and program X-001 (Lonza Bioscience). After 16 h cells were treated with 100 nM dex or veh for four hours. RNA was isolated with the RNeasy Mini extraction kit (Qiagen, 74104) according to the manufacturer's instructions.

cDNA conversion and qPCR

cDNA was generated using two gene specific primers for plasmid GFP and RPL19 as endogenous control (key resources table) and the Quantitect Reverse Transcriptase (Qiagen) kit following manufacturer's instructions. Regulatory elements activity was assessed with qPCR using primers for RPL19 and GFP (key resources table). The qPCR was analysed with the relative quantification method and GFP expression was normalized over the RPL19 expression. Data are shown both as expression values (2^{-DCt}) and as fold changes of the expression values (dex/veh).

Mendelian randomization analysis (Mra) and Phenome-wide association (PheWAS) study

All processing and analysis were conducted using R software.[100] To assess the potentially causal effect of ZBTB16 on a range of phenotypes, rs648044 was used as genetic proxy with log fold-changes of the effect allele (A), averaged over STARR-qPCR experiments, (β= 1.475794, SE= 0.1015) used as exposure effect and variance estimates.

Outcome phenotype selection

Outcome phenotypes were selected from the MRC IEU OpenGWAS platform focusing on phenotype batches originating from the UK Biobank study, the NHGRI-EBI GWAS Catalog, and a GWAS on brain imaging phenotypes based on UK Biobank data (Table S7).[96,101,102] From the initial phenotype list originating from these batches, 8979 phenotypes from GWAS of European populations were selected after filtering out duplicates and phenotypes not of interest to this study (e.g., "Patient Care Technician *responsible for patient data*" *or "Day-of-week questionnaire completion requested"*). Duplicates were filtered using a semi-automated procedure including deletion of phenotypes with identical names and smaller GWAS sample size as well as manual filtering of phenotypes with high similarity in trait names (quantified using the restricted Damerau-Levenshtein distance >0.8 implemented in the stringdist package).[103] This procedure resulted in a final phenotype list of 7,503 phenotypes.

Mendelian armonizedon analysis (Mra)

The *TwoSampleMR* package was used for Mra.[104] Outcome data for rs648044 were extracted from phenotype summary data, which were available for 7,323 outcomes, and effect and reference alleles were armonized with exposure data. Wald ratio Mra estimation was applied as method of choice for single-SNP Mra for all remaining outcome phenotypes.[105] To account for the multiple comparisons, P-values from all 7,323 comparisons were corrected using the Benjamini-Hochberg method.[106]

Illustration of PheWAS associations

Significant phenome-wide associations with brain region phenotypes were illustrated by overlaying human brain atlas regions as proxies of the regions of interest onto the MNI template in MRIcroGl (version v2.1.58-0, https://www.nitrc.org/projects/mricrogl/). Due to the different analysis streams and granularities of the significant brain phenotypes, different atlases were used to portray the results. For illustration purposes, regions taken from probabilistic atlases were thresholded at 10%. As a proxy for the circular anterior insular cortex thickness, we used the anterior insula of the "Hammersmith atlas[107]". Medial lemniscus, cingulate gyrus part of cingulum, cingulum hippocampus, uncinate fasciculus, posterior limb of internal capsule, inferior fronto-occipital fasciculus, uncinate fasciculus, anterior corona radiata and the corticospinal tract were portrayed using the JHU ICBM DTI 81 white matter labels,[108] the acoustic radiation was visualized using the Juelich histological atlas,[108] the inferior longitudinal fasciculus, and the thalamic radiation by the JHU White Matter Tractography[109] and the superior thalamic radiation by the XTRACT HCP Probabilistic tract atlas.[110]

Scripts and data for the Mra-PheWAS analyses are openly available via https://osf.io/4ud6q/ for full transparency.

InTraUterine prospective pregnancy cohort study

Study Cohort

The InTraUterine sampling in early pregnancy (ITU) is a prospective pregnancy cohort study with the overarching aim to unravel maternal-placental-fetal mechanisms involved in the programming of health and disease.[53] It comprises 943 women and their singleton children born alive in Finland between 2012–2017. The women were recruited at the voluntary national 21-trisomy screen, offered to all pregnant women at gestational weeks 9 to 21. Of these women, 543 (57.6%) were referred for fetal chromosomal testing at Helsinki and Uusimaa Hospital District Fetomaternal Medical Center (FMC) and thereafter cleared for fetal chromosomal abnormality. The rest, 400 (42.4%) women, had a negative 21-trisomy screen result and were not referred for fetal chromosomal testing.

Ethics approval

The ITU study was conducted according to the World Medical Association's Declaration of Helsinki and the research protocol was approved by the ethics committee of the Helsinki and Uusimaa Hospital District (approval date: 06.01.2015, reference number: 269/13/03/00/09). All women provided written informed consent. In compliance with the General Data Protection Regulation of the European Union, the personal data of all participants were de-identified, protected at all times, and confidentiality agreements were signed by all personnel with ITU data access.

Data availability

A complete set of salivary cortisol, fetal rs648044 genotype (genotype frequencies of AA = 0.234, GG = 0.284, AG = 0.482, Hardy-Weinberg-Equilibrium [HWE] p = .630), and child neuropsychological assessment at 35.6 months of age (range 24.5 to 42.5) was available for 246 mother-child dyads (46.7% female sex) before and for 221 mother-child dyads (49.1% female sex) after gestational week 28.

Salivary cortisol assessment

Salivary cortisol sample collection, storage, and competitive enzyme immunoassay were previously described.[52] Briefly, mothers collected saliva in early (<22 weeks, T1), mid- (22-35 weeks, T2), and late pregnancy (≥36 weeks, T3) when waking up (S1), 15 (S2) and 30 min (S3) thereafter; at 10 am (S4), noon (S5), 5 pm (S6), and when going to sleep (''lights out'', S7). Gestational week at assessment was computed using the ultrasound-based date of conception and self-reported date of cortisol assessment.

Salivary cortisol samples were available for 690 women (307 with and 383 without chromosomal testing) of which 15 were excluded due to corticosteroid treatment[111] resulting in a total of 9,992 (70.49%) out of the maximum number of 14,175 samples in 675 women. Samples measured in duplicate were averaged and those with a coefficient of variation greater than 0.25 (1.6%, 164/9,992) excluded. Cortisol values below the lower limit of the assay range were truncated at 0.05 μg/L (2.4%, 240/9,992, no values fell above the upper limit). For some women, multiple assessment days (i.e., 24) fell into the same pregnancy stage and only the one with most complete observations, protocol adherence, or absence of day-specific outliers (i.e., >2 SD of the day-specific mean) was kept, leading to the exclusion of 159 samples. For 6 women, date records were missing, and their 89 samples were excluded. Further exclusion criteria were self-reported illness on the day of sampling (89 samples, leading to the exclusion of all samples of 2 women), getting up before the first sample (108 samples), sampling of S2 or S3 more than 60 min after awakening (10 samples), or S4 sampling within the first 60 min after awakening (17 samples). Missing sampling times (0.1%, 19/9,992) were imputed according to sampling protocol for S2 to S6 or sample median for S1 and S7. The distribution of the cortisol samples was positively skewed, and thus natural log+1 transformed. To further reduce skewness, outliers (i.e., >4 SD pregnancy stage-specific mean) were winsorized (9 samples).

The resulting dataset consisted of 9,356 samples from 667 women (292 with and 375 without chromosomal testing). Of these, 589 provided salivary samples before gestational week 28 (range 12.3 to 27.9 weeks) and 499 after gestational week 28 (range 28.14 to 41.3 weeks). Total cortisol output per pregnancy stage was estimated based on the area under the curve with respect to ground (AUCg) of all seven saliva samples using the trapezoid rule.[112] When multiple occasions fell into the same gestational interval (i.e., gestational week <28 or >28 weeks), the total cortisol output and gestational week at assessment were averaged.

Fetal genotypes

DNA was extracted from cord blood leucocytes using a bead-based method optimised by tissue type (Chemagic 360, Perkin Elmer) and genotyping performed on Illumina GSA-24v2-0 A1 arrays according to the manufacturer's guidelines. Genotyping quality control and imputation were previously described in Kvist et al.[53] In total, the rs648044 genotype was available for 446 (genotype frequencies of AA = 0.226, GG = 0.285, AG = 0.489, HWE p = .704) out of a maximum of 944 samples.

Child neuropsychological assessment

At 35.48 months (range 24.5 to 42.5 months) follow-up, children's cognitive skills were assessed by trained psychology students (supervised by a clinical pediatric neuropsychologist) using the Bayley-III screening test.[113] The Bayley-III is a norm-referenced test designed to identify infants and toddlers at risk for developmental delay. Scores were calculated using normative data tailored for exact age, with higher scores indicating better performance. The Bayley cognitive assessment was available for n = 618 (50.5% female) out of a maximum of 944 children. Neurodevelopmental delay was defined as 1 SD below the sample mean.

Maternal and child covariates

All mothers consented to link their data to Finland's detailed nationwide registers. Maternal sociodemographic and pregnancy characteristics used in this study included maternal age at delivery [years], parity [nulli-/multiparous], whether the mother was referred for fetal chromosomal testing [yes vs no], maternal education [primary/applied university/university education], which was self-reported in early pregnancy, and pre-pregnancy Body Mass Index [BMI, weight (kg)/height^2 (m^2)] verified by measurement in the first antenatal clinic visit between 7-10 gestational weeks. Child characteristics included gestational age at delivery and child sex.

Logistic regressions

Binomial logistic regressions were run using the ''glm'' function of the ''stats'' package in R (version 3.6.1).[100] We tested the association of the interaction effect of mean cortisol * rs648044 A allele on delay in cognitive performance as defined by the Bayley cognitive subscale, using the following covariates: gestational week at cortisol assessment, child sex, child age when the Bayley questionnaire was done, gestational age at birth, maternal age and education, parity, maternal body mass index and case vs control as women were either recruited at routine care (controls) or after referral for chromosomal testing (cases). Cases all tested negative for chromosomal abnormality). The plot on Figure 7E was done using the ''ggplot2'' package[114] in R.

QUANTIFICATION AND STATISTICAL ANALYSIS

Image analysis and quantifications

Immunostained fluorescent stainings were visualized using a Leica laser-scanning microscope and analysed with FIJI ((Fiji Is Just) ImageJ 2. 1. 0/1.53c; Java 1. 8. 0_172 [64 bit]).[60] For analysis of the hCOs, we included ventricles that fulfilled the following criteria: clear ventricular structure with elongated, radially-organized cells surrounding the ventricular zone (VZ- determined with DAPI staining), at least one cell electroporated in the VZ (for electroporation experiments) and expression of PAX6 and EOMES to define dorsal cortical ventricles. In addition, we stained with EMX1 to ensure the dorsal telencephalic identity of our ventricles/hCOs (Figure S2L). Cell counting was performed in one representative plane of a z stack using the cell counter tool in FIJI. For electroporations binning analysis was done.

Electroporations on hCOs

For each experiment, at least seven independent ventricles from five different HPS0076-hCOs generated in three independent preparations grown in different times were analysed. Analysis of the ZBTB16 phenotype in the electroporation experiments was performed by always comparing hCOs electroporated with ZBTB16-F2A-GFP plasmid vs F2A-GFP control plasmid in the same batches. Throughout the area of the electroporation, bins were set as follows: the maximal distance between the most migrated GFP-positive cell and the apical surface of the ventricle where the first GFP-positive cells are located was measured and divided into three equally-heighted bins. Bin A is mainly comprised of the VZ, bin B of the outer-most basal part of the VZ and the SVZ and bin C of the CP. As normalization we used the number of GFP-positive cells in total or per bin as specified in each section.

For the GFP cell morphology reconstructions, the afore-mentioned electroporated ventricles were re-imaged with a step size of 0.2 μm to ensure that we captured the whole cell including its processes. The tracking of the cells was done using the SNT plugin[115] of ImageJ on the 3D images. In total, 34 GFP-electroporated cells and 22 ZBTB16-GFP- electroporated cells were traced.

Dexamethasone effects on hCOs

For each experiment, at least twelve independent ventricles from six different HPS0076-hCOs and at least five independent ventricles from three different No.1-hCOs, generated in two independent preparations for HPS0076 and in one preparation from No.1 iPSCs grown in different times were analysed. For analysis of the dex effects in hCOs, VZ and SVZ (subventricular like-zone) were defined by the cell shape and proximity to the apical zone. The VZ area presented elongated, radially-organized cells positive for radial glia markers (PAX6, SOX2) but not for basal progenitors' markers (EOMES). The area on top, assigned as SVZ, was positive for EOMES. Areas were defined and measured in FIJI using the ROI Manager tool. As normalization we used the surface of the measured area. For the quantification the PAX6 zone thickness in Figure S1C we measured the length of the PAX6+ zone and normalized that to the total length of the germinal zone (defined by radially placed DAPI+ nuclei) and the length of the cortical plate (defined by BCL11B+ staining). For each ventricular structure we analysed at least 3 different sides of it and averaged the results in order to account for intra-ventricle variations. For Figures S1C and S4A we quantified the thickness of the germinal zone, as defined by elongated and radially placed DAPI+ nuclei, and the thickness of the PAX6 zone, as defined by PAX6 positive staining, in all ventricles that were quantified in Figure 1B and Figure 3D respectively.

In utero *electroporations of fetal mice*

For each experiment and condition, at least eight mouse cortical sections from five different embryos collected from two mothers were analysed. The GFP- and ZBTB16-GFP plasmids were electroporated in different embryos of the same mother. For analysis of the *in utero* electroporations in mice, we used binning analysis. We chose a cortical column that had the majority of electroporated cells and we set the bins as follows: the maximal distance between the most migrated GFP-positive cell in the cortical plate and the apical surface of the ventricle was measured and divided by five. The width of the bin was the width of the 40x lens image and it was the same for all sections and mice. As normalization we used the number of GFP-positive cells in total or per bin as specified in each section.

Statistics & plots

The statistical analysis was performed in GraphPad Prism (Version 9. 1.0 (2021)). Groups were then compared with a two-tailed Mann-Whitney test or a one-way or a two-way ANOVA with multiple comparisons corrected with the two-stage step-up method of Benjamini, Krieger and Yekutieli,[75] according to the type of data and their distribution. More specifically, p-values for Figures 1F, 3E, 3F, 4C, 4E, 4G, 5C, 5E, 5F, and 7B and for Figures S1A–S1C, S2C, S2E, S4A, S4F, S5B, S5D, S6B, S6D, S6F, S6G,S6I,S6K–S6N, and S7A, S7B, S7E, and S7F were calculated using two-way ANOVA with Benjamini, Krieger and Yekutieli multiple testing correction. P-value for Figures 2F and 6B were calculated using one-way ANOVA with Benjamini, Krieger and Yekutieli multiple testing correction. P-values for Figures 1C, 2E, 3C and for Figures S2H, S2J, S2K, S3H, S3J, and S7C were calculated using Mann–Whitney (two-tailed) comparison between the two treatment/electroporation groups (veh-dex or ZBTB16 overexpression plasmid- control plasmid). P-value for Figure S4C was calculated with a Fisher's exact test. On the plots, the p-values depicted are the Mann-Whitney comparison p-value or for the ANOVAS the corrected post-hoc p-values. For each statistical test the N equals the dots depicted in each plot.

Dots in plots of Figures: 1C&F, 3C,E&F and of Supplemental Figures S1A–S1C, S2J, S2K, S3J, S4C, S4F, S5B, and S5D represent individual ventricles. Specifically, for HPS0076 hCOs results in Figures 1C and 1F and for Figures S1A and S1B dots represent individual ventricles from six different HPS0076-hCOs generated in two independent preparations grown in different times. For No.1 hCOs results in Figures 1C and 1F dots represent individual ventricles from three different No.1-hCOs generated in one preparation. For Figures 3C,3E, and 3F and for Figure S4F dots represent individual ventricles from at least five different HPS0076-hCOs generated in three independent preparations grown at different times. For Figures S2J, S2K, S3J dots represent individual ventricles from three different hCOs generated in two independent preparations per iPSC line grown at different times. For Figure S5 dots represent individual ventricles from 4 different hCOs per condition and per genotype generated in one preparation for each genotype.

Dots in plots of Figures 2E, 7F, 4E, 4G, and 7B and of Figures S2C, S2E, S3H, S8B, S8C, S8E, and S8F represent replicates each containing RNA/DNA/protein/cells extracted from a pool of two to three organoids each, i.e, 3 pools each containing 2 to 3 organoids so 6 to 9 organoids in total. More specifically, dots and western lanes in Figures 2E, 2F and 4B represent protein and RNA expression values from an isolate of a pool of three hCOs each. The hCOs were generated in two independent preparations grown in different times per iPSC line. For Figures 4E and 4G dots represent FCa results from an isolate of a pool of two hCOs each. The hCOs were

generated in two independent preparations per iPSC line grown at different times. For Figure 7B and for Figure S7B results of two or three replicates for dex respectively and 3 for dmso are depicted and they represent methylation levels from an isolate of a pool of two hCOs each. For Figures S2C, S2E, and S2H dots represent FCa results from an isolate of a pool of two hCOs each. The hCOs were generated in one preparation for panel 2E and in two preparations for panel 2C and 2H. For Figures S3H dots represent RNA expression values from an isolate of a pool of two hCOs each. The hCOs were generated in two independent preparations grown in different times per iPSC line. For Figures S7E and S7F dots represent RNA expression values or fold changes from an isolate of a pool of two hCOs each. The hCOs were generated in one preparation per iPSC line.

Dots in plots of Figures 5 and S6 represent individual embryos. Each dot represents average counts from at least two cortical sections from one embryo. Embryos collected from two independent mothers were analysed for each staining.

For Figure 6 dots represent luciferase activity values of cells from independent cell culture wells for each condition and promoter.

Dots in Figures S7B and S7C represent RNA expression values or fold changes from isolates of independent cell culture wells for each genotype and treatment.

Box and whisker plots represent 25th to 75th percentile of the data with the center line representing the median and whiskers representing minima and maxima. Bar plots with error bars showing standard error of the mean (SEM). Plots and statistics for all figures were generated using the GraphPad Prism 9 software.

Significance: ****$p \leq 0.0001$, ***$p \leq 0.001$, **$p \leq 0.01$, *$p \leq 0.05$, ns $p > 0.05$.